

Age of anatexis in the crustal footwall of the Ronda peridotites, S Spain

Journal Article**Author(s):**

Acosta-Vigil, Antonio; Rubatto, Daniela; Bartoli, Omar; Cesare, Bernardo; Meli, Sandro; Pedrera, Antonio; Azor, Antonio; Tajčmanová, Lucie

Publication date:

2014

Permanent link:

<https://doi.org/10.3929/ethz-a-010735954>

Rights / license:

[In Copyright - Non-Commercial Use Permitted](#)

Originally published in:

Lithos 210-211, <https://doi.org/10.1016/j.lithos.2014.08.018>

Funding acknowledgement:

335577 - Interplay between metamorphism and deformation in the Earth's lithosphere (EC)

1 **Age of anatexis in the crustal footwall of the Ronda peridotites, S Spain**

2 Antonio Acosta-Vigil^{a,*}, Daniela Rubatto^b, Omar Bartoli^c, Bernardo Cesare^c, Sandro Meli^d,

3 Antonio Pedrera^a, Antonio Azor^e, Lucie Tajcmanova^f

4 ^a Instituto Andaluz de Ciencias de la Tierra, Consejo Superior de Investigaciones Científicas-Universidad de

5 Granada, Avenida de las Palmeras 4, 18100 Armilla, Granada, Spain

6 ^b Research School of Earth Sciences, The Australian National University, Canberra, Australia

7 ^c Dipartimento di Geoscienze, Università di Padova, Padova, Italy

8 ^d Dipartimento di Fisica e Scienze della Terra “Macedonio Melloni”, Università di Parma, Parma, Italy

9 ^e Departamento de Geodinámica, Universidad de Granada, Granada, Spain

10 ^f Department of Earth Sciences, Swiss Federal Institute of Technology, Zurich, Switzerland

11 * Corresponding author. Tel.: +34 958 230000 ext. 190033; fax: +34 958 552620.

12 E-mail address: aacosta@ugr.es (A. Acosta-Vigil)

13 * Corresponding author. Tel.: +34 958 230000 ext. 190033; fax: +34 958 552620.

14 E-mail address: aacosta@ugr.es (A. Acosta-Vigil)

15 **Abstract**

16 This study investigates the age of anatexis of a crustal sequence constituting the footwall of
17 the Ronda peridotite slab, in the hinterland of the Betic Cordillera (S Spain, region of Istán).

18 These rocks represent a polymetamorphic basement involved in the Alpine orogeny and show

19 an increase in the proportion of melt towards the peridotites. Metamorphic conditions in the

20 migmatites vary between $T \approx 675-750$ °C at $P \approx 0.30-0.35$ GPa. The timing of metamorphism

21 and deformation of the migmatites around the Ronda peridotites is controversial and has been

22 previously ascribed to either the Alpine or Variscan orogenies. We present U-Pb SHRIMP

23 dating of zircons from six samples collected across the migmatitic sequence that provide a

24 tighter age constraint on the metamorphism. Zircon ages are related to conditions of

25 metamorphism on the basis of the relationships between zircon microstructures and degree of
26 melting recorded by the host rocks. Anatexis occurred during the late stages of the Variscan
27 orogeny ($\approx 280\text{-}290$ Ma), as indicated by ages of euhedral, oscillatory-zoned domains or new
28 crystals in metatexites and diatexites. Thin, U-rich zircon rims that are affected by radiation
29 damage yield discordant scattered dates between $\approx 260\text{-}30$ Ma, which are interpreted as
30 reflecting a thermal and fluid overprint during the Alpine orogeny that produced
31 recrystallization and Pb loss in Permian zircons. This study identifies a previously unknown
32 Variscan domain within the Betic Cordillera, and indicates, in accordance with previous
33 studies, that Variscan basements recycled during the Alpine orogeny that formed the Betic
34 Cordillera preserve pre-Alpine mineral associations and tectonic fabrics.

35 *Keywords:* U-Pb zircon SHRIMP dating, crustal anatexis, Ronda peridotite, Betic
36 Cordillera

37 **1. Introduction**

38 Determining the ages and rates of high-grade metamorphism and anatexis in poly-
39 metamorphic terrains is hampered by a series of factors. First, minerals and/or single mineral
40 domains that crystallized and equilibrated during tectonometamorphic events belonging to
41 different orogenic cycles can coexist within a sample (e.g. Fernández-Suarez et al., 2002).
42 Second, the geochronometers that are suitable at upper amphibolite- and granulite-facies
43 conditions are mostly accessory minerals such as zircon and monazite, whose growth is
44 difficult to relate to major mineral assemblages that provide P-T conditions. Confusion or lack
45 of information on the relationships between radiometric ages and major mineral growth
46 produces a great uncertainty in the P-T-time path and, hence, in the tectonic interpretation of
47 poly-metamorphic terrains. In the case of accessory minerals, the link between ages and
48 metamorphic mineral assemblages can be achieved by different approaches, such as: (i)
49 combined ages of accessory mineral and P-T data from garnet, through the study of mineral

50 inclusions in the garnet and the partitioning of REE between garnet and the accessory
51 minerals (Rubatto, 2002; Hermann and Rubatto, 2003; Whitehouse and Platt, 2003; Harley
52 and Kelly, 2007); (ii) *in situ* dating of accessory minerals that show well-defined
53 microstructural relationships with major mineral assemblages (Williams and Jercinovic,
54 2012); (iii) dating of accessory minerals that can be linked to particular metamorphic
55 reactions (Janots et al., 2009); and (iv) relating microstructures and ages of accessory minerals
56 with variation in metamorphic grade in the host rock (Rubatto et al., 2001; Williams, 2001) or
57 directly with melt inclusions (Cesare et al., 2003, 2009).

58 The Ronda peridotites outcrop in the hinterland of the Alpine Betic Cordillera of south
59 Spain (Fig. 1), and represent the largest known exposure of subcontinental lithospheric mantle
60 (Obata, 1980). They constitute a tectonic slab up to ≈ 5 km thick, sandwiched in between
61 crustal units that show increasing metamorphic grade towards the contact with the mantle
62 rocks, reaching conditions of anatexis at several hundred meters from the contact (Lundeen,
63 1978; Balanyá et al., 1997; Tubía et al., 1997; Acosta et al., 2001; Argles et al., 1999; Platt et
64 al., 2003a; Esteban et al., 2008). Partial melting in the crustal footwall has been associated
65 with the hot crustal emplacement of the Ronda peridotites (Torres-Roldán, 1983; Tubía et al.,
66 1997, 2013; Esteban et al., 2008), whereas anatexis of the crustal rocks above the peridotite
67 has been related to decompression melting during crustal thinning (Argles et al., 1999; Platt et
68 al., 2003a). Numerous studies conducted in the area (or in equivalent units from the Rif in
69 northern Morocco) have attributed the high-grade metamorphism and partial melting in these
70 rocks, and in general in the crystalline basements of the Betic-Rif orogen, either to the
71 Variscan (Michard et al., 1997; Acosta, 1998; Bouybaouène et al., 1998; Sánchez-Rodríguez
72 1998; Montel et al., 2000; Rossetti et al., 2010) or the Alpine (Loomis, 1975; Sánchez-
73 Rodríguez and Gebauer, 2000; Whitehouse and Platt, 2003; Rossetti et al., 2010; Esteban et
74 al., 2011a) orogenies. This controversy obviously makes uncertain the P-T conditions reached

75 during the Alpine orogeny, the geodynamic evolution of the entire Betic-Rif orogen, and even
76 the age of the crustal emplacement of the Ronda peridotites. This study sheds light on this
77 controversy by investigating the age of zircon in rocks across the anatectic sequence that
78 underlies the Ronda peridotites. To relate ages from zircons to P-T conditions derived from
79 the major mineral assemblages in the rocks, we have studied the changes in microstructures
80 and ages of zircons collected along a cross-section perpendicular to the main foliation in the
81 migmatites and the contact between peridotites and migmatites.

82 **2. Geological setting**

83 The Betics in southern Spain and the Rif in northern Morocco constitute an arcuate
84 orogenic belt, known as the Gibraltar arc (Fig. 1). This belt formed during Alpine times due to
85 N-S to NW-SE convergence of the Iberian and African plates, coeval to westward migration
86 of the so-called Alborán continental domain (Andrieux et al., 1971; Balanyá and García-
87 Dueñas, 1987; Sanz de Galdeano, 1990). The Alborán domain represents the metamorphic
88 hinterland of the orogen, whereas the foreland is constituted by Triassic to Early Miocene
89 sedimentary rocks deposited on the Iberian and African continental margins. Details
90 concerning the precise paleogeographic location of the Alborán domain and the tectonic
91 processes that produced the orogen are still unclear (e.g. Platt et al., 2013). Most authors do
92 agree, however, that the Alborán domain underwent crustal thickening and metamorphism
93 during two major successive Alpine events: (i) accretion of materials in a subduction zone
94 located somewhere to the east of the present-day location of Iberia, from Early-Middle
95 Eocene to Late Oligocene-Early Miocene times; and (ii) subduction-underthrusting of the
96 southern Iberian and northern African continental margins beneath the Alborán domain and
97 their subsequent collision in the Early Miocene, which also generated the Gibraltar arc (Platt
98 et al., 2013, and references therein). The subduction and collision process produced thin-
99 skinned tectonics in the foreland. Concomitantly with this collision, the Alborán domain

100 underwent thinning at its back, generating the Alborán Sea (Galindo-Zaldívar et al., 1998;
101 Comas et al., 1999). This thinning was probably associated with the roll back of an east-
102 dipping subducting oceanic slab that has been imaged by seismic tomography studies (Blanco
103 and Spakman, 1993; Pedrera et al., 2011; Alpert et al., 2013).

104 Based on lithostratigraphic and metamorphic criteria, structural units within the Alborán
105 domain have been grouped into three stacked tectonic complexes. In the Betic Cordillera,
106 these complexes are, from bottom to top, the Nevado-Filábride, Alpujárride and Maláguide
107 (Fig. 1). Middle Miocene (17-15 Ma) ages for the HP-LT metamorphic event in the Nevado-
108 Filábride (López-Sánchez Vizcaino et al., 2001; Platt et al., 2006) suggest that this complex is
109 a slab of the Iberian margin that underthrusts the Alborán domain during the Early Miocene
110 collision. The Maláguide complex (Blumenthal, 1930; Foucault and Paquet, 1971) is made of
111 Early Paleozoic to Eocene rocks (Martín-Algarra et al., 2000). Although all materials are
112 strongly deformed by thrusts and folds, Permo-Triassic to Eocene rocks appear
113 unmetamorphosed and lie unconformably on the pre-Permian basement. The latter is affected
114 by a low-grade metamorphism towards the bottom of the sequence, interpreted as Variscan in
115 age (Martín-Algarra et al., 2009).

116 The rocks studied in this contribution pertain to the Alpujárride Complex, whose tectonic
117 units include, from top to bottom: Triassic carbonates, Permo-Triassic phyllites and quartzites
118 (these lithologies constitute the post-Variscan sedimentary cover, e.g. Martín and Braga,
119 1987), and a pre-Mesozoic crystalline basement made of graphitic mica schists, gneisses and
120 migmatites (e.g. Egeler and Simon, 1969). All these rocks have been deformed and
121 metamorphosed, and record nearly adiabatic decompressional P-T paths from medium-high-
122 to low-pressure conditions (e.g. Torres-Roldán, 1981; Goffé et al., 1989; Tubía and Gil-
123 Iburguchi, 1991; García-Casco and Torres-Roldán, 1996; Azañón et al., 1997). A penetrative
124 foliation that postdates the medium-to-high-pressure mineral assemblage and predates a later

125 low-pressure assemblage, has been traditionally associated with pervasive ductile thinning of
126 the Alpine orogenic pile, producing the telescoping of the medium-to-high-pressure isotherms
127 and associated apparently high thermal gradients (Torres-Roldán, 1981; Azañón et al., 1997;
128 Balanyá et al., 1997; Platt et al., 2003a). Metamorphism and deformation recorded by
129 Alpujárride rocks have been attributed to the Alpine crustal thickening of the Alborán domain
130 during orogenic accretion (e.g. Platt et al., 2013). This conclusion is based on the presence of
131 Triassic carbonates at the top of the sequence, the existence of high-pressure metamorphism,
132 the apparent continuity between structures in the sedimentary cover and crystalline basement,
133 and results from some geochronological studies (see below). After thinning and during the
134 late metamorphic stages, a new contractional event produced folding and thrusting of the
135 original Alpujárride slab, generating an imbricated stack of units showing top-to-the-N sense
136 of displacement (Simancas and Campos, 1993). During this stage, metamorphic
137 recrystallization took place mostly at the contacts between units, producing a penetrative
138 crenulation cleavage. Previous isotherms were therefore folded and, in the imbricated stack of
139 units, higher-grade rocks from the lower part of the sequence were thrust and superposed over
140 lower-grade rocks.

141 **3. Metamorphism in the Alpujárride units in the vicinity of the Ronda peridotites**

142 The metamorphic grade of the Alpujárride units increases from east to west in the orogen
143 and, in the western Betics, the base of the sequence incorporates granulitic migmatites and
144 even slices of subcontinental mantle, i.e. the Ronda peridotites (Fig. 1). In the vicinity of the
145 peridotites, the Alpujárride crustal rocks show systematically the highest metamorphic grade
146 and extensive melting (Obata, 1980; Torres-Roldán, 1983; Balanyá et al., 1997; Tubía et al.,
147 1997; Argles et al., 1999; Acosta-Vigil et al., 2001; Esteban et al., 2008). Los Reales and
148 Blanca constitute the two westernmost and highest-grade Alpujárride units (Hoepfener et al.,
149 1964; Mollat, 1968; Navarro-Vilá and Tubía, 1983). Los Reales is a strongly condensed, 5

150 km-thick, crustal section recording an increasing metamorphic grade, from unmetamorphosed
151 and greenschist-facies carbonates and phyllites at the top (though recording pressures of 0.7-
152 0.8 GPa, at 200-350 °C), to greenschist and amphibolite-facies schists towards the middle, and
153 granulite-facies felsic gneisses at the bottom (with pressures up to 1.3-1.4 GPa, at 700-800 °C)
154 (Torres-Roldán, 1981; Platt et al., 2003a). The Ronda peridotites constitute the base of the
155 Los Reales nappe and are separated from the overlying granulitic gneisses by a ductile shear
156 zone (Balanyá et al., 1997; Platt et al., 2003a).

157 The peridotite slab is located on top of the Blanca unit, which has been subdivided in the
158 Ojén and Guadaiza units. Both of these units are characterized by an inverted metamorphism
159 with granulite-facies rocks on top and amphibolite-facies rocks at the bottom. However, these
160 two units show differences in pressure, lithology and *P-T* path, and the relationship between
161 them is unclear. In the Ojén unit, ≈300 m of metasedimentary Grt-Crd-Sil mylonites (mineral
162 abbreviations after Kretz, 1983), recording peak conditions of ≈0.8 GPa and 800 °C, are at the
163 contact with the peridotites (Tubía et al., 1997). They grade downwards into compositionally
164 equivalent Grt- and Crd-bearing pelitic and quartzo-feldspathic diatexites and metatexites that
165 have not been affected by the mylonitic fabric (Acosta, 1998; Acosta-Vigil et al., 2001). The
166 bottom of the sequence is constituted by amphibolite-facies Sil-bearing schists and marbles
167 (Westerhof, 1977; Tubía, 1988). Metatextitic migmatites include amphibolite lenses that
168 preserve eclogitic boudins, recording peak conditions of 1.7 GPa and 800 °C (Tubía and Gil-
169 Ibarra, 1991). The protolith of the amphibolites intruded the metasedimentary sequence
170 ≈184 m.y. ago, during the break up of Pangea and the opening of the Neotethys between
171 Africa and Iberia (Sánchez-Rodríguez and Gebauer, 2000). Conversely, the Guadaiza unit is
172 formed by a much thinner (tens of m) and lower pressure mylonitic band at the contact with
173 the peridotites. Below the mylonites there is a 100-200 m thick sequence of low pressure Crd-
174 Sil-And bearing migmatites (equilibrated at 0.4-0.6 GPa and 800 °C), and Grt-St-Sil-And-Crd

175 greenschists- to amphibolite-facies schists of unknown thickness, since they constitute the
176 structurally lowest outcropping level (Torres-Roldán, 1983; Tubía 1988; Acosta, 1998;
177 Esteban et al., 2008; Tubía et al., 2013). In contrast with the rest of Alpujárride units
178 (including Ojén), *P-T* paths determined in the mylonites and migmatites of the Guadaiza unit
179 are characterized by heating at low pressure (Esteban et al., 2008; this work). Furthermore,
180 the Guadaiza unit contains two rock types that have not been described in the Ojén unit: the
181 Istán orthogneiss and some very peculiar pelitic diatexites (Acosta, 1998; this work). We have
182 investigated the microstructures and ages of zircons collected across the migmatitic sequence
183 of the Guadaiza unit, from metatexites located far from the contact with the Ronda peridotites,
184 to nebulites and schlieric diatexites close to the contact with the ultramafic rocks.

185 **4. Previous geochronological data**

186 Medium to high-grade Alpujárride rocks throughout the Betic-Rif orogen have been dated
187 using a variety of isotopic systems (Table 1). Alpine ages ($\approx 18-50$ Ma) have been mostly
188 yielded by isotopic systems with medium to low closure temperatures ($\leq 600-650$ °C): K-Ar
189 and Rb-Sr analyses on whole rock, muscovite, biotite and hornblende, and zircon and
190 monazite fission-tracks. Uranium-Th-Pb dating of monazite and zircon provided a range of
191 older ages, from $\approx 280-320$ Ma (Variscan) to $\approx 560-640$ Ma (Cadomian or Pan-African), 940-
192 1020 Ma (Grevillian), and even Early Proterozoic to Early Archean. Ages of >500 Ma have
193 been interpreted as inherited from the source rocks of the Alpujárride sequence. Alpine and
194 Variscan ages have been related to metamorphic events affecting partially or totally the
195 Alpujárride sequence during these orogenic cycles. Hence, metamorphic assemblages in these
196 rocks have been ascribed by different authors to one or both of these orogenies. The main
197 reason for the controversial interpretation on the age of metamorphism is the difficulty of
198 relating radiometric ages to crystallization of major minerals. The spread of Alpine ages (18-
199 50 Ma) has been explained as recording different stages of the orogeny. There is uncertainty

200 in the age of the high-pressure metamorphism related to the generation of the crustal wedge
201 between ≈ 50 -30 Ma (Platt et al., 2005). The ages of 22-18 Ma are mostly interpreted as
202 recording a main extensional episode responsible for ductile-to-brittle thinning of the orogenic
203 pile. Because U-Pb in zircon and thermochronometers with a large range in closure
204 temperatures (≈ 600 to 100 °C) all return ages of 22-18 Ma, it has been proposed that during
205 this period the metamorphic pile cooled at high rates due to rapid extension and exhumation
206 (e.g. Zeck et al., 1989a, 1992; Monié et al., 1994; Andriessen and Zeck, 1996; Platt et al.,
207 2003b).

208 Loomis (1975) first reported K-Ar ages of ≈ 30 -81 Ma on whole rock and biotite
209 concentrates from diatexites of the Guadaiza unit (outcrops of Estepona and Guadaiza, Fig. 1,
210 Table 1). More recent U-Pb zircon studies from single samples within the migmatitic
211 sequence of Guadaiza and Ojén have provided both Variscan and Alpine ages. These studies,
212 however, have not been able to differentiate between Variscan and Alpine mineral
213 assemblages and fabrics. Thus, U-Pb ages on single zircon crystals from a diatexite of
214 Guadaiza (Estepona) yielded Variscan ages of ≈ 315 -319, 324 and 335 Ma (Acosta, 1998).
215 Sánchez-Rodríguez (1998) first used cathodoluminescence (CL) images of zircon from
216 Alpujárride rocks to guide SHRIMP dating, and reported U-Pb ages of zircons from a
217 diatexite of the Guadaiza unit (Guadaiza), an undeformed pegmatitic vein within mylonites,
218 and a banded migmatite (likely a metatexite), both from the Ojén unit (locality Albornoque).
219 Inherited cores provided concordant ages at ≈ 2700 , ≈ 580 and ≈ 490 Ma. Oscillatory-zoned
220 overgrowths yielded discordant ages between ≈ 277 -60 Ma, with upper and lower intercepts of
221 ≈ 291 -306 and 20 Ma, respectively. Very thin (< 30 μm) and unzoned zircon rims yielded
222 scattered dates between ≈ 134 -21 Ma. Thin zircon rims were also dated from a leucocratic
223 gneiss of the Guadaiza unit right underneath the Ronda peridotites (locality Carratraca) and
224 returned a range of U-Pb SHRIMP dates between 255-20 Ma (Platt and Whitehouse, 1999).

225 Recently, Esteban et al. (2011a, 2011b) dated zircons from mylonites of the Guadaiza unit,
226 located at the contact and far from the contact with the Ronda peridotites (localities Guadaiza
227 and Yunquera, respectively), and metaquartzites layers within marbles and schists of the Ojén
228 unit (locality Albornoque). They obtained U-Pb SHRIMP ages of ≈ 2700 , ≈ 2200 , ≈ 1200 and
229 ≈ 650 Ma for the cores, and 20-43 Ma for the thin unzoned rims.

230 **5. Methods**

231 *5.1. Whole rock analyses*

232 The minimum amount of material collected during field work for chemical analyses was
233 about 8 to 10 kg per sample. Powders with a grain size ≤ 25 μm were obtained by crushing
234 and grinding the samples using a crusher with hardened still jaws and a tungsten carbide jar,
235 respectively. Bulk rock major element and Zr analyses were conducted by X-Ray
236 fluorescence using an automated Philips PW1404 spectrometer at the Centro de
237 Instrumentación Científica (CIC), Universidad de Granada. The analyses were done on glass
238 beads made by fusing the rock powder mixed with $\text{Li}_2\text{B}_4\text{O}_7$. Precision was $\pm 1\%$ for SiO_2 ,
239 Al_2O_3 , TiO_2 , FeO^* , CaO , K_2O and P_2O_5 , and $\pm 3\%$ for Na_2O , MnO , MgO and Zr (for Zr
240 concentrations of ≈ 100 ppm). Trace element analyses were obtained by ICP-MS at the CIC,
241 after HNO_3 -HF digestion of 0.1000 g of sample powder in a Teflon-lined vessel at 180 °C and
242 $\approx 1.38 \cdot 10^6$ Pa during 30 min., evaporation to dryness, and subsequent dissolution in 100 ml of
243 4 vol.% HNO_3 . The measurements were carried out with a PE SCIEX ELAN-5000
244 spectrometer. Precision at 1σ confidence level was $\approx \pm 2\%$ and $\pm 5\%$ for concentrations of 50
245 and 5 ppm, respectively.

246 *5.2. Mineral analyses*

247 Major minerals were analyzed with a Cameca SX-50 electron microprobe at the University
248 of Oklahoma. Matrix reduction used the PAP correction algorithm (Pouchou & Pichoir,

249 1985). Minerals were analyzed using an accelerating voltage of 20 kV, a beam current of 10
250 nA, and a 3 μm spot size. Counting times were 30 s on peak for all elements except Ca, Ba, Sr
251 and Fe; Ca, Ba and Sr were counted for 45 s, and Fe was counted for 60 s.

252 5.3. *Pseudosection modeling*

253 The diatexitic migmatite Ista-16 (see below) was used for phase equilibria modeling. Due
254 to the presence of Mn-rich Grt in some of the studied rocks (see below), the calculation was
255 done in the MnO-Na₂O-CaO-K₂O-FeO-MgO-Al₂O₃-SiO₂-H₂O-TiO₂ (MnNCKFMASHT)
256 chemical system by the Gibbs energy minimization (Connolly, 2009) with the thermodynamic
257 database of Holland and Powell (1998, as revised in 2003). We used the solution model of
258 melt from White et al. (2007), of garnet from Holland and Powell (2001), of biotite from
259 Tajčmanová et al. (2009), of white mica from Coggon and Holland (2002), of plagioclase
260 from Newton et al. (1980) and of K-feldspar from Thompson and Hovis (1979). An ideal
261 model was used to account for the solutions of Mn in ilmenite and cordierite. The amount of
262 H₂O component involved in the calculation for the bulk rock composition was assumed as the
263 loss of ignition of XRF analysis. The XRF bulk-rock composition (in mol %) used for
264 calculation is indicated in the upper left inset of the calculated *P-T* phase diagram sections
265 (see below).

266 5.4. *Cathodoluminescence imaging and U-Pb dating of zircons*

267 Zircons were separated after rock crushing using conventional heavy liquid and magnetic
268 techniques. The grains were mounted in epoxy resin and polished down to expose the near
269 equatorial sections. Cathodoluminescence imaging was carried out on a HITACHI S2250N
270 and a Jeol JSM-6610 scanning electron microscopes supplied with an ellipsoidal mirror for
271 CL at the ANU in Canberra. Operating conditions for the SEM were 15 kV/60-70 μA and 20
272 mm working distance.

273 Uranium-Th-Pb analyses were performed with the sensitive high resolution ion microprobe
274 (SHRIMP II) at the Australian National University in Canberra. Instrumental conditions and
275 data acquisition were as described by Williams (1998). The data were collected in sets of six
276 scans throughout the masses and a reference zircon was analyzed each fourth analysis.
277 Uranium-lead data were collected over three analytical sessions with 2σ calibration errors
278 between 1-2.3%, which was propagated to single analyses. The measured $^{206}\text{Pb}/^{238}\text{U}$ ratio was
279 corrected using reference zircon from the Temora granodiorite (TEM1, Black et al., 2003).
280 The fraction of non-radiogenic ^{206}Pb (f_{206}) was calculated from the measured $^{207}\text{Pb}/^{206}\text{Pb}$
281 ($^{7/6}\text{R}_m$) and the non-radiogenic $^{207}\text{Pb}/^{206}\text{Pb}$ ($^{7/6}\text{R}_c$) according to Williams (1998), i.e $f_{206} =$
282 $(^{7/6}\text{R}_m - ^{7/6}\text{R}^*) / (^{7/6}\text{R}_c - ^{7/6}\text{R}^*)$, where $^{7/6}\text{R}^*$ is the expected radiogenic $^{207}\text{Pb}/^{206}\text{Pb}$ assuming
283 concordance at the approximate age of the sample. The $^{7/6}\text{R}_c$ composition was assumed to be
284 that predicted by Stacey and Kramers (1975) model.

285 Data evaluation and age calculation were done using the software Squid 1 and Isoplot/Ex
286 (Ludwig, 2003), respectively. Single ages quoted in the text are $^{206}\text{Pb}/^{238}\text{U}$ ages $\pm 1\sigma$, unless
287 otherwise specified. Average ages are quoted at 95% confidence level. Uncertainties on
288 average ages were increased to 1% whenever necessary to account for external errors.

289 **6. Migmatitic sequence of Guadaiza: field relationships, petrography and geochemistry**

290 Neither the migmatitic sequence nor the internal structure of the Guadaiza unit have been
291 previously described in detail, and hence we report below comprehensive field, structural,
292 petrographic and geochemical observations. We have investigated the Guadaiza migmatitic
293 sequence outcropping near the town of Istán, and provide a detailed NW-SE cross-section
294 perpendicular to both the main fabric in the migmatites and the contact between peridotites
295 and migmatites (Fig. 2). Samples of the several identified rock types have been collected for
296 the U-Pb dating of zircons, and their structural position is projected on the cross-section of
297 Fig. 2. Some samples were not strictly collected along the A-A' cross-section marked in Fig.

298 2, because either some areas were not accessible or the quality of the outcrops was
299 significantly better in other adjacent areas. Nevertheless, the collected samples correspond to
300 the rock types and structural positions marked in the cross-section. We use in this article the
301 revised definition of migmatite proposed by Sawyer (2008), i.e. a genetic, partial-melting-
302 based definition that include descriptive terms for the principal parts of the migmatite such as
303 leucosome, melanosome, paleosome and neosome. Readers are referred to Sawyer (2008)
304 regarding these terms as well as the morphological types of migmatites used in the description
305 below.

306 The Guadaiza unit consists of an inverted metamorphic sequence with quartzitic schists at
307 its base and migmatites of quartzofeldspathic or metapelitic composition on top. The
308 thickness of the migmatitic sequence is \approx 350-400 m. The term migmatite is applied to rocks
309 above the schists because these rocks are found in a medium-to-high grade metamorphic area,
310 are heterogeneous and contain locally derived former melt (see below). As in many regionally
311 metamorphosed terrains partial melting occurred during deformation, producing a variety of
312 somewhat complex relationships between foliations and melt-rich domains.

313 *6.1. Schist-migmatite contact*

314 The schists are overlain by partially melted gneisses that, on the basis of field appearance
315 and bulk composition (see below), we interpret as orthoderivate (the Istán orthogneiss; see
316 also Acosta, 1998). The proportion of former melt in these quartzofeldspathic rocks increases
317 towards the contact with the Ronda peridotites, with transition to an anatectic granite near the
318 contact (Fig. 2). The contact between schists and orthogneisses is sharp and parallel to the
319 main regional foliation. In some places, late normal and strike-slip faults omit the highest-
320 grade schists. The schists consist of alternating quartzitic and pelitic bands, have a pelitic bulk
321 rock composition (Ista-12, Table 2), and are made of
322 Qtz+Bt+Pl+Sil+Grt+St+Crd+And+Tur+Gr. The main foliation in the schists (S_p) is defined

323 by the alignment of Bt and Sil, whereas Grt, St, Pl and And are wrapped by S_p (see also
324 Tubía, 1988; Esteban et al., 2008). This foliation has a dominant NE-SW strike and generally
325 dips moderately (10-30°) to the SE, though it is affected by cm- to dm-scale isoclinal to tight
326 N-vergent folds with trends ranging from NE-SW to E-W and sub-horizontal axes (Fig. 2).

327 6.2. *Metatextitic migmatites*

328 The orthogneiss located above the schists has a granitic *sensu stricto* bulk composition
329 (Ista-9 and Ista-15, Table 2) and show a glandular, porphyroblastic structure due to the
330 presence of abundant cm-sized and variably deformed (prismatic to *augen*) crystals of Kfs,
331 enclosed in a fine-to-medium-grained matrix (Figs. 3a-b). The main foliation (S_p) visible in
332 the field is defined by alternation of Bt-rich folia and quartzofeldspathic layers. S_p is affected
333 by folds similar in orientation and, apparently, geometry as well, to those in the underlying
334 schists (Figs. 3a-b). Sometimes a N-S to NW-SE lineation, marked by Sil on foliation planes,
335 is visible in hand specimen (Fig. 2), and inspection under the microscope shows that folds
336 affecting S_p have associated some S-C microstructures indicating an apparent top-to the N-
337 NW sense of shear (Fig. 3c). This metagranitic rock is made of
338 Qtz+Kfs+Pl+Bt+Sil+And+Ms+Chl, with accessory Ilm+Ap+Zrn+Mnz. S_p , S and C are
339 defined by oriented Bt, Sil, And and porphyroblasts of Pl. Alkali feldspar ($Or_{67-92}-Ab_{32-7}$),
340 frequently perthitic, shows as 0.2-1 mm subhedral to anhedral crystals or prismatic to *augen*
341 porphyroblasts up to several cm in length. Plagioclase ($Ab_{80-88}-An_{18-9}$) forms either 0.2-1 mm
342 subhedral crystals or porphyroblasts of 1 mm wrapped by Sil±Bt folia; this relict Pl includes
343 oriented Bt and Sil prisms (Fig. 3d). Biotite ($Mg\#\approx 0.28-0.29$) shows as either anhedral
344 crystals frequently intergrown with fibrolite in 1-2 mm long aggregates that define S_p , S and
345 C, or 0.1-0.5 mm euhedral and non-oriented crystals. Sillimanite mostly form oriented
346 fibrolite mats that define S-C microstructures or, more rarely, small individual needles
347 included in porphyroblasts of Pl. Andalusite forms anhedral elongated crystals parallel to S_p ,

348 wrapped by and transformed to $\text{Sil}\pm\text{Ms}\pm\text{Qtz}$ (Fig. 3e). Muscovite is sparse and occurs as
349 anhedral crystals replacing feldspars and And, within $\text{Bt}\pm\text{Sil}$ aggregates, or as rare relict
350 grains within feldspars. Chlorite is rare and replaces Bt. It is difficult to ascertain if this rock
351 preserves any of the original minerals/mineral domains pertaining to the former granite, other
352 than the large Kfs which may represent former megacrysts (Fig. 3a). Andalusite, large Kfs,
353 porphyroblasts of Pl and their Sil and Bt inclusions, all wrapped by S_p , constitute the earliest
354 minerals present in this rock. Biotite and fibrolite crystallized (or recrystallized) during
355 deformation and generation of S_p , S and C. Despite the penetrative planar structure, most
356 feldspars in the matrix are not deformed and microstructures indicative of the former presence
357 of melt, such as subhedral microstructure and cusped Qtz and feldspars, are abundant (Fig.
358 3f; see Brown et al., 1999; Sawyer, 2001; Vernon, 2011). These textural observations indicate
359 that this rock was partially melted during folding of S_p and development of S-C
360 microstructures. The assemblage during the anatectic event was composed of melt, residual
361 Bt, Sil and, likely, residual Qtz and feldspars as well. Former melt shows now as euhedral Bt,
362 subhedral Kfs and Pl, and cusped Qtz and feldspars (Fig. 3f). During a late retrograde stage,
363 Ms and Chl replaced feldspars, And and Bt. Only Qtz records some later intra-crystalline
364 deformation shown by undulose extinction, development of subgrains and presence of sutured
365 grain boundaries.

366 The main foliation of the orthogneiss is also defined in the field by abundant cm-to-dm
367 Grt-bearing leucocratic bands roughly parallel to the Bt-rich folia (Ista-7 and Ista-14 in Table
368 2, and Ist-6; Figs. 4a-c). These bands can be affected by decametric folds similar in geometry
369 and orientation to those described by S_p (compare Figs. 3a-b and Fig. 4a). In detail, the
370 contact between leucocratic bands and orthogneiss is irregular (Fig. 4c) and may be associated
371 with mm-thick bands of Bt-rich folia. These leucocratic bodies are thicker in fold hinges (Fig.
372 4b). Grt-bearing bands are mostly made of $\text{Qtz}+\text{Kfs}+\text{Pl}+\text{Grt}+\text{Ms}+\text{Sil}+\text{Tur}$, and have

373 leucogranitic compositions that plot in the vicinity of the 500 MPa H₂O-undersaturated
374 haplogranite eutectics in a pseudoternary Qtz-Or-Ab normative diagram (Fig. 5). There is
375 petrographic continuity (i.e. there is no major mineralogical or microstructural discontinuity;
376 e.g. Brown, 2008) between the orthogneiss and leucocratic bands, and the transition between
377 them is marked by the appearance of Mn-rich Grt (Alm₇₄-Py₀₂-Grs₀₂-Sps₂₂) and almost
378 complete disappearance of Bt. Garnet in these bands forms 0.1-5 mm euhedral to subhedral
379 crystals crowded with $\leq 5 \mu\text{m}$ inclusions and wrapped by Sil folia (Figs. 4d-e). Some of these
380 inclusions are euhedral, polycrystalline and show negative crystal shape (see inset in Fig. 4e),
381 and may correspond to crystallized melt inclusions or nanogranites (Cesare et al., 2011).
382 Inclusions of crystals or polycrystalline aggregates of Qtz are also frequent (Fig. 4e).
383 Sillimanite forms elongated and oriented fibrolite mats (Figs. 4d-e). K-feldspar (Or₇₄₋₈₉-Ab₂₆-
384 ₁₁) and Pl (Ab₉₀₋₉₆-An₀₇₋₀₂) form 0.5-2 mm euhedral to subhedral crystals; Kfs also shows as
385 large cm-sized perthitic megacrysts (Or₆₅-Ab₃₅) (Fig. 4c). Tourmaline forms either 1-5 mm
386 euhedral crystals or 0.1-0.5 mm anhedral crystals. Frequent subhedral Ms and rare relict And
387 are also present. Despite their orientation parallel to S_p, presence of oriented fibrolite and
388 some deformation of Qtz (undulose extinction, development of subgrains and sutured grain
389 boundaries), this rock commonly shows a subhedral microstructure (Fig. 4f). This igneous
390 microstructure, together with the bulk leucogranitic composition, shows that Grt-bearing
391 bands represent former melt-rich domains. Based on the irregular boundaries and petrographic
392 continuity with the orthogneiss (except for the presence of Grt), the igneous microstructure,
393 and relationships with S_p, Grt-bearing layers are interpreted as melt produced during the
394 anatexis of the orthogneiss, right before or during the syn-anatectic deformation that produced
395 folding of S_p and development of S-C microstructures. Garnet is not present in the orthogneiss
396 and microstructures suggest that this mineral did not crystallize from the melt (Figs. 4d-e);
397 hence, Grt likely represents a peritectic mineral. Despite the presence of some residuum (Grt

398 and fibrolite), Grt-bearing layers are named leucosomes (hereafter Grt-leucosomes), whereas
399 the Bt-rich bands at the rims of some Grt-leucosomes constitute melanosomes, and the host
400 orthogneiss represents the paleosome (see Sawyer, 2008).

401 The main foliation is locally obliterated by cm-to-dm Crd-bearing leucocratic and
402 undeformed patches, mostly made of Qtz+Kfs+Pl+Crd+Sil+Tur+Ms, that also have a
403 leucogranitic composition and plot very close to the 500 MPa H₂O-undersaturated
404 haplogranite eutectics (Ista-13 in Table 2, and Ist-10; Figs. 5, 6a-b). The boundary between
405 orthogneiss and Crd-bearing patches is irregular and diffuse, and there is petrographic
406 continuity between them. The transition is marked by the appearance of Crd and
407 disappearance of Bt. Cordierite forms either 0.1-5 mm euhedral to subhedral crystals or mm-
408 to-cm rounded/elongated aggregates with abundant inclusions of Qtz and poikilitic to skeletal
409 microstructure (Figs. 6a-c, 6e). Cordierite may appear homogeneously distributed throughout
410 the entire patch or concentrated at the center (Figs. 6a-b). Some Crd crystals may be wrapped
411 by Sil folia (Fig. 6c). Garnet is rare within these leucocratic patches; subhedral to anhedral
412 crystals, similar in microstructure to those in Grt-leucosomes, have been found as inclusions
413 in Pl (Fig. 6d). Sillimanite forms elongated and at times oriented fibrolite mats (Figs. 6c, 6e).
414 Plagioclase (Ab₇₉₋₉₀-An₁₉₋₀₉) shows as 0.1-2 mm euhedral to subhedral crystals, and Kfs (Or₇₈-
415 ₉₁-Ab₂₁₋₀₉) forms 0.1-1 mm subhedral to anhedral crystals (Figs. 6e-f). Despite the presence of
416 oriented Sil and some subsolidus deformation marked by the undulose extinction and sutured
417 grain boundaries of Qtz, Crd-bearing patches have an igneous subhedral microstructure (Figs.
418 6e-f). Hence, they represent former melt-rich domains that, based on the field relationships
419 and petrographic continuity (except for the presence of Crd), we interpret as melt produced
420 during anatexis of the orthogneiss after the folding of S_p and generation of Grt-leucosomes.
421 Cordierite is abundant in the leucocratic pods and absent in the orthogneiss, and
422 microstructures suggest that at least a proportion of this mineral did not crystallize from the

423 melt (Fig. 6c). Hence, Crd likely represents a peritectic phase, and we name the Crd-bearing
424 patches as neosomes (hereafter Crd-neosomes). The leucocratic part of these neosomes,
425 formed by Qtz+Pl+Kfs, constitutes the leucosome, and most Crd and Sil represent the
426 melanosome. The compositions of both Grt-leucosomes and Crd-neosome differ slightly from
427 that of the orthogneiss (Table 2, Fig. 5): compared to the latter, Grt-leucosomes and Crd-
428 neosome project closer to the haplogranite eutectics and have lower concentrations in FeO_t,
429 MgO, TiO₂ and Rare Earth Elements, lower ASI [=moles (Al₂O₃/(CaO+Na₂O+K₂O))] values,
430 and higher concentrations in Na₂O. This indicates that during their genesis there was some
431 compositional segregation of the original orthogneiss.

432 Because the orthogneiss partially melted, but the proportion of melt was not high enough
433 as to obliterate its pre-partial melting structure (S_p), this rock represents a metatexitic
434 migmatite that, depending on the melting stage to which we refer, can be classified either as
435 stromatic to fold structured migmatite (with respect to Grt-leucosomes) or patch migmatite
436 (with respect to Crd-neosomes).

437 6.3. Diatexitic migmatites

438 At approximately 100 m from the contact with the schists, migmatites show an increase in
439 the proportion of Crd-neosomes (and therefore melt), the pre-partial melting structure of the
440 rock starts to disappear, and abundant, large and somewhat rotated dm-to-m rafts of
441 orthogneiss are included in a matrix of Crd-neosome. Concomitantly, a magmatic foliation
442 defined by elongated Crd aggregates develops in the rock. Migmatites at this level can be
443 classified as schollen migmatites (Figs. 7a-b).

444 In the upper 250-200 m of the migmatitic sequence the proportion of neosome increases
445 and dominates volumetrically over the paleosome, whereas the pre-partial melting structure is
446 only visible in rare, rounded and small (cm-scale) fragments of orthogneiss included in a
447 granitic looking Crd-rich rock. At 250-200 m from the contact with the peridotites,

448 migmatites are massive and do not show a clear planar fabric, hence they are classified as
449 diatexite migmatites. Some of them show higher proportions of Crd and Bt, with these
450 ferromagnesian minerals homogeneously distributed, and have granitic bulk compositions
451 very similar to the orthogneiss; these can be classified as mesocratic diatexites (Ista-16, Table
452 2; Figs. 5 and 7c-d). Others are leucocratic, show a heterogeneous distribution of rounded Crd
453 aggregates and have leucogranitic compositions; these can be classified as leucocratic
454 diatexites (Ist-14, Fig. 7e). Both diatexite types contain
455 Qtz+Pl+Kfs+Crd+Bt+Ms+Sil+And+Ilm±Tur, and show a typically igneous subhedral
456 microstructure with no signs of subsolidus deformation (Fig. 7f). Cordierite ($Mg\# \approx 0.35-0.38$)
457 shows as either euhedral to subhedral 0.5-1 mm crystals, or poikilitic to skeletal mm-to-cm
458 aggregates intergrown with, or rich in inclusions of Qtz. Plagioclase ($Ab_{71-90}-An_{27-08}$) forms
459 0.1-0.5 mm euhedral to subhedral crystals, and Kfs ($Or_{67-83}-Ab_{32-16}$) shows as either 0.5-1 mm
460 subhedral to anhedral crystals, or cm-sized prismatic megacrysts. Subhedral to anhedral Bt
461 ($Mg\# \approx 0.29-0.32$) is more abundant in the mesocratic diatexites, whereas Ms is more frequent
462 in the leucocratic diatexites, where it seems to be a product of retrograde reaction between
463 melt, Als and Kfs, as it includes fibrolite mats, And and Kfs. Sillimanite is scarce and
464 commonly forms fibrolitic mats that may be intergrown with $Bt \pm Pl \pm And$, similar to
465 microstructures observed in the orthogneiss. Andalusite is also scarce and appears both as
466 isolated subhedral squares/prisms, or anhedral crystals partially transformed to Sil and/or Ms.
467 Tourmaline shows as a late intergranular phase, commonly replacing Crd. Based on these
468 microstructures, we interpret that mesocratic and leucocratic diatexites were constituted by a
469 large proportion of melt, peritectic Crd, and residual Bt and scarce Sil and And. Also, there
470 was likely some residual Qtz and feldspars, as shown by the rare fragments of orthogneiss.
471 Upon cooling, melt crystallized to euhedral-subhedral feldspars, Qtz and likely some Bt, Crd

472 and Tur; Ms formed by reaction between melt, Als and Kfs; and Tur formed by reaction
473 between an evolved B-rich melt and Crd,

474 At \approx 100-150 m from the contact with the Ronda peridotite migmatites show a strong
475 magmatic foliation and/or a cm-to-dm flow banding dipping moderately to the SW (Ist-17B,
476 Fig. 7g), indicating that they are structurally below the peridotites. These rocks can be
477 classified as schlieric migmatites. In the studied cross-section, these rocks are mostly quartzo-
478 feldspathic in composition and similar in mineralogy and microstructures to the previously
479 described diatexite migmatites. In fact, the magmatic banding is formed by alternating
480 mesocratic and leucocratic diatexites (Figs. 7c-e). Under the microscope, the schlieric
481 diatexites are undeformed and show subhedral microstructures (Fig. 7h); flow banding is due
482 to variations in the proportion of Crd and Bt.

483 Close to the peridotites (at a few tens of meters) the migmatites appear darker and consist
484 of some peculiar diatexites of pelitic composition (Sba-30, Table 2; this sample has been
485 collected from equivalent rocks in the outcrop of Estepona, Fig. 1), made of a fine-to-
486 medium-grained granitic matrix that includes Kfs megacrysts, Qtz nodules and cm-to-dm
487 rounded rafts of mostly residuum (see also Esteban et al., 2008). Morphologies vary from
488 diatexite migmatites (massive and undeformed) to schlieric migmatites (showing a magmatic
489 foliation defined by the orientation of Kfs and rafts of melanosome). The matrix of this
490 peculiar rock is an anatectic Crd-Bt granite with subhedral microstructure (Pl, Kfs and Crd are
491 euhedral to subhedral), whereas rafts of melanosome are made of a low pressure granulitic
492 assemblage of Pl+Crd+Sil+Hc+Bt, with Sil delineating a relict foliation. In the studied area,
493 the contacts between these pelitic diatexites, the underlying quartzo-feldspathic schlieric
494 migmatites, and the overlaying peridotites, are brittle post-metamorphic faults. Figure 8
495 shows the relationships between all described rock types, and presents a schematic evolution

496 of the Istán migmatites with increasing time and temperature and decreasing distance with the
497 peridotite contact.

498 **7. *P-T* estimates and conditions of anatexis**

499 The Istán orthogneiss has a complex geologic history, and the study of its earliest stages is
500 beyond the scope of this contribution. We choose as starting point the generation of And, one
501 of the earliest minerals present in the rock. The relict And wrapped by fibrolite, presence of
502 abundant Crd, together with results from pseudosection modeling (Fig. 9), indicate that the
503 orthogneiss was heated at low pressure from the And field ($P \leq 0.30$ GPa and $T \leq 650$ °C).
504 Metatexites with Grt-leucosomes and Crd-neosomes formed above the solidus at $T \geq 675$ -680
505 °C. Grt-leucosomes formed first at temperatures of ≈ 675 -685 °C, after crossing the solidus
506 and before entering the Grt-out fields. Crd-neosomes started to generate after entering the
507 Crd-present fields and Grt-out region, at $T \approx 700$ -710 °C. Crd-neosomes increased in
508 proportion with increasing T , to form the diatexites. Mesocratic, leucocratic and schlieric
509 diatexites close to the contact with the peridotites, constituted by melt, peritectic Crd, residual
510 Bt and likely some residual Qtz and feldspars as well, generated at $T \leq 750$ °C (at $P \leq 0.35$ -0.30
511 GPa), as Grt is absent in these rocks. Tubía (1988) reported conditions of equilibration in the
512 schists of 0.35-0.45 GPa and 525-550 °C which, because the orthogneiss is above the solidus,
513 should correspond to $P-T$ of schists located at some distance from the orthogneiss in the
514 original metamorphic sequence. Previous studies of the pelitic diatexites located at the contact
515 with the peridotites determined the following $P-T$ conditions, which are in accordance with
516 our estimations: 0.30-0.50 GPa and 750-800 °C at Estepona (Torres-Roldán, 1983); 0.55-0.65
517 GPa and 675-750 °C at Istán (Esteban et al., 2008).

518 Heating of these rocks took place at pressures below the “invariant” melting point I_3 of
519 Thompson and Algor (1977), and the dehydration of Ms necessarily occurred before crossing
520 the wet solidus. Hence, melting could have occurred at the wet granite solidus in the presence

521 of H₂O-rich fluids and/or during the progressive fluid-absent breakdown melting of Bt (see
522 Bartoli et al., 2013). The low proportion of hydrous minerals in the orthogneiss, relatively low
523 T of melting for the generation of diatextitic migmatites, and lack of melanosomes associated
524 with Crd-leucosomes, all point to water-fluxed melting (e.g. Sawyer, 2010; Brown, 2013).
525 However, and although a detailed analysis of the mechanisms of melting is beyond the scope
526 of this contribution, the following observations suggest that anatexis may have occurred
527 largely through biotite dehydration melting: (i) anatexis at high water activities and in the
528 presence of strongly peraluminous minerals (Als, Crd) should produce melts with high ASI
529 and Na/K ratios (Patiño-Douce and Harris, 1998; Acosta-Vigil et al., 2003); (ii) Crd-
530 neosomes and, particularly Grt-leucosomes contain anhydrous peritectic minerals (Grt, Crd)
531 and show low ASI values and high K₂O concentrations; (iii) Grt-leucosomes and Crd-
532 neosomes project in the vicinity of the H₂O-undersaturated haplogranite eutectics (Fig. 5); (iv)
533 mesocratic diatexites reached P-T conditions well above the wet granite solidus and close to
534 the Bt-out reaction (Fig. 9).

535 **8. Zircon microstructures and ages**

536 Zircons in all samples contain several textural domains (Fig. 10). Common to all samples
537 is the presence of anhedral cores with complex and variable zoning. They are interpreted to be
538 inherited and were only occasionally analyzed. They yield variably discordant ages from ~300
539 Ma to 2.5 Ga (²⁰⁷Pb/²⁰⁶Pb ages, see Supplementary Table 1 for details). Most analyses were
540 done on the external portion of the crystals and are described below in detail, grouped by
541 sample type.

542 *8.1. Paleosome Ista-9, Grt-leucosome Ist-6 and Crd-neosome Ist-10*

543 Zircons from paleosome, leucosome and neosome show similar internal zoning (Fig. 10).
544 Oscillatory-zoned, euhedral domains that can include an inherited core and are generally
545 overgrown by dark rims, yield scattered dates between 284-226 Ma (Fig. 11). The Th/U of

546 these domains is 0.07-0.33 (Supplementary Table 1), significantly higher than in the rims.

547 Most grains have euhedral rims that are dark in CL. The rims are extremely rich in U
548 (2300–7200 ppm), low in Th/U (0.02–0.01) and show signs of radiation damage: mottled
549 appearance, frequent inclusions and porosity (Fig 10). U-Pb dates for the rims are largely
550 discordant, scattering between 187–30 Ma (mostly >50 Ma). The reliability of these dates will
551 be discussed below.

552 8.2. Mesocratic diatexite Ista-16 and schlieric migmatite Ist-17B

553 Oscillatory zoned domains overgrow the detrital cores and yield mostly concordant ages
554 around 280–290 Ma but with some scattering up to 300 Ma and down to 190 Ma. The main,
555 statistically consistent group of analyses define an age of 289.6 ± 2.9 Ma for mesocratic
556 diatexite Ista-16 and 283.8 ± 2.8 Ma for schlieric migmatite Ist-17B (Fig. 11). The U content of
557 these domains is moderate to high (200-1350 ppm) and the Th/U is generally low (0.03-0.07).

558 A darker rim that show oscillatory or no zoning is present in some crystals. These rims can
559 either form embayments in texturally older domains or grow in apparent texturally continuity
560 with the ~290-280 Ma zircon. For these darker rims, U contents are very high (3300-5300
561 ppm), Th/U is low and dates scatter from 270 to 100 Ma (Ista-16), and from 240 to 30 Ma
562 (Ist-17B). Due to the unclear textural relationships and size of the darker rims, some of these
563 analyses are possibly mixed between different textural domains.

564 8.3. Leucocratic diatexite Ist-14

565 The leucocratic diatexite, outcropping in between diatexites Ist-16 and Ist-17B, contains
566 zircons that are similar to those of the paleosome, leucosome and neosome described above.
567 Thick CL dark rims that show oscillatory zoning or mottled appearance (Fig. 10) grow directly
568 on the detrital cores or on oscillatory zoned domains. Mainly dark rims were analyzed in this
569 sample and they are extremely rich in U (3500-7200 ppm) and yield discordant dates
570 scattering between 246-34 Ma (Fig. 11).

571 **9. Discussion**

572 *9.1. Age of anatexis and metamorphism in the Guadaiza unit*

573 Zircon across the prograde anatectic sequence of the Guadaiza unit at Istán shows a
574 heterogeneous population of inherited cores (variable ages, zoning patterns, and Th-U
575 concentrations; Figs. 10 and 11, Supplementary Table 1). We do not attempt to interpret this
576 limited dataset of scattering and partly discordant core dates.

577 Euhedral, oscillatory-zoned domains grew directly on the inherited cores or formed new
578 crystals in mesocratic diatexite Ista-16 and schlieric migmatite Ist-17B, the samples that
579 experienced the highest degree of partial melting. These domains are characterized by
580 moderate U content (100 to 1000 ppm) and generally low Th/U (mostly <0.1), and yield an
581 age of 289.6 ± 2.9 Ma (Ista-16) and 283.8 ± 2.8 Ma (Ist-17B). A similar domain has been
582 analyzed occasionally in other migmatites (Ista-9, Ist-6 and Ist-10). The euhedral shape and
583 zoning in these domains suggest crystallization in a melt, and the low Th/U indicates that a
584 Th-rich phase (likely monazite) was stable during zircon growth. These microstructures and
585 compositions are consistent with anatexis (e.g. Rubatto et al., 2001; Williams, 2001, Rubatto
586 et al., 2013) and therefore we conclude that the migmatitic sequence formed at around 280-
587 290 Ma during the very final stages of the Variscan orogeny.

588 In all migmatite samples (except mesocratic diatexite Ista-16), the most external zircon
589 domain is a CL-dark, U-rich rim with weak zoning and euhedral shape. The boundary
590 between the 280-290 Ma domains and the dark rim is parallel to the zoning, although cross
591 cutting relationships are also observed (Fig. 10). Measured U-Pb dates on these rims scatter
592 widely between ~260 and 30 Ma (Fig. 11). Three competing effects prevent age determination
593 of these domains. (i) The rims show evidence of significant radiation damage including
594 porosity, trails of micro inclusions and patchy (disturbed) CL-zoning (Fig. 10). Such textures
595 have been described in zircons from granitic and metamorphic rocks (e.g. Pidgeon, 1998) and

596 investigated experimentally (Geisler, 2003). Significant radiation damage is to be expected in
597 zircon with such extreme U contents (2000-7000 ppm) and, if the zircon is subject to any
598 thermal overprint and/or fluid alteration, the damaged domain will be strongly affected by Pb
599 mobilization and loss (Pidgeon, 1998; see also Zeck and Whitehouse, 2002; Rossetti et al.,
600 2010). This in turn leads to the partly reset and discordant U-Pb dates that scatter between
601 ~260 and 30 Ma. For such domains it is only possible to give a minimum age assuming that
602 the oldest measured date was least affected by Pb loss. (ii) Additionally, accuracy of ion
603 microprobe analyses are compromised by the matrix effect associated with analyzing zircons
604 with U content above 2000-3000 ppm (Butera et al., 2004; Hermann et al., 2006; White,
605 2012). SHRIMP analyses of U-rich zircons are systematically biased to older apparent dates,
606 proportionally to the U content of the zircon. In zircons with 7000 ppm the measured date is
607 expected to be biased between ~5 and 15% towards older values (Hermann et al., 2006;
608 White, 2012), i.e. between ~15 and 40 Ma. (iii) It cannot be excluded that the most external
609 part of the U-rich rim is of Alpine age and that analyses partly overlap with this younger rim.

610 Overall, the zircon U-Pb analyses, excluding the inherited cores older than 300 Ma, show a
611 rough inverse correlation between U content and measured date (Fig. 12). The analyses on
612 zircon domains that have a moderate U content, and whose measured date is likely unaffected
613 by radiation damage and matrix effects, are mainly around 280-290 Ma. The higher the U
614 content the younger is the measured date. This correlation, together with textural
615 observations, suggests that the U-rich rims also formed during Permian anatexis, or soon
616 after, and underwent significant Pb loss during a later overprint favoured by radiation damage.
617 Due to the incompatible nature of U, low degree melting in the presence of monazite will
618 produce high U and low Th/U melts (Stepanov et al., 2012; see also Acosta-Vigil et al., 2010),
619 and in turn U-rich zircons. This is in line with the observation that U-rich zircon rims are
620 particularly abundant in the metatexites compared to diatexites, i.e. in the migmatites showing

621 a lower degree of melting. A possible thermal and fluid overprint of the migmatite sequence
622 during the Alpine orogeny might have further enhanced recrystallization and Pb loss in the U-
623 rich zircon rims. The youngest date measured at ~30 Ma is proposed as a maximum age for
624 this overprint.

625 *9.2. Age of high-grade metamorphism in the Alpujarride complex and emplacement of the*
626 *Ronda peridotites*

627 Regional high temperature metamorphism and anatexis of an orthogneiss in the early
628 Permian (280-290 Ma) is in line with previous U-Pb zircon ages for the Guadaiza, Ojén, and
629 Torrox high-grade rocks, and granulites and gneisses from Beni Bousera (Acosta, 1998;
630 Sánchez-Rodríguez, 1998; Zeck and Whitehouse, 1999; Rossetti et al., 2010) (Table 1).
631 Sánchez-Rodríguez (1998) dated Variscan zircon domains that are euhedral and oscillatory
632 zoned in metasedimentary migmatites from Guadaiza and Ojén, and argued for crystallization
633 of the anatectic major mineral assemblage that forms the rock at ~300 Ma. Similarly to our
634 study, Sánchez-Rodríguez (1998) obtained an array of discordant zircon dates from ~300 Ma
635 to 20 Ma, which were interpreted as due to recrystallization and partial Pb loss from the
636 Variscan domains. In the central Betics, Zeck and Whitehouse (1999) studied the Torrox
637 gneiss at the base of the Torrox Alpujarride unit. They considered an orthoderivate origin for
638 this rock and assigned the euhedral and oscillatory zoned Variscan zircon domains
639 overgrowing inherited cores to the crystallization of its granitic protolith (that formed Kfs, Pl,
640 Qtz, Bt) and the residual crystals of And. These authors did not observe zircon rims of Alpine
641 age, and concluded that zircon was not involved in the Alpine recrystallization of the granite.
642 In a later study of zircons from an amphibolite-facies schist from an Alpujarride unit in the
643 eastern Betics, Zeck and Williams (2001) also found good evidence of metamorphism at 305 ± 3
644 Ma and scarce rims rich in U and common Pb, with scattering dates (3 analyses) around 20
645 Ma. Rossetti et al. (2010) dated zircons from both leucosomes and sheets of slightly

646 discordant peraluminous granites within deformed felsic granulites above the Beni Bousera
647 peridotites, in northern Morocco. They concluded that the Variscan sector- and oscillatory-
648 zoned domains of zircons from leucosomes and granitic dikes were coeval to the tectonic
649 fabrics, metamorphism and anatexis in the host granulites. Structureless zircon rims with
650 Alpine dates were observed in some samples, and interpreted as re-equilibration of Variscan
651 domains during the early Miocene.

652 An alternative, Alpine age for the migmatization has been proposed on the basis of mostly
653 thin and structureless Alpine euhedral zircon rims from high-grade rocks located both above
654 and below the Ronda peridotites (Platt and Whitehouse, 1999; Whitehouse and Platt, 2003;
655 Esteban et al., 2011a). Whitehouse and Platt (2003) investigated zircon in felsic granulitic
656 gneisses above the peridotites as a function of microstructural location (crystals in the matrix
657 versus crystals included in Grt cores and rims), and the distribution of trace elements between
658 zircon and garnet. They used partitioning of REE between these minerals to relate growth of
659 Miocene zircon rims to garnet rims in the granulitic gneisses (Los Reales unit, Carratraca),
660 thus arguing for high-grade mineral assemblages of Alpine age. However, no age data for the
661 garnet was obtained, and the zircon/garnet trace element partitioning calculated for the
662 Carratraca sample differs from what measured in other granulites (e.g. Hermann and Rubatto,
663 2003), leaving open the possibility that the garnet is pre-Alpine. Esteban et al. (2011a) have
664 also used the concordant ages of ≈ 22 Ma obtained on the thin zircon rims in the Guadaiza
665 migmatites located right below and at the contact with the peridotites, to conclude that
666 anatexis and deformation of these rocks are Alpine.

667 A solution to this apparent controversy in the Alpujarride units of the central and western
668 Betics stems from the work of Zeck and Whitehouse (1999, 2002), who distinguished
669 between two high-grade Alpujarride mineral assemblages and attributed the first one to the
670 Variscan orogeny (porphyroclasts wrapped by the main foliation) and a later assemblage to

671 Alpine overprint (minerals defining the main foliation). Based on field and petrographic data,
672 Zeck and Whitehouse (1999) interpreted the Torrox gneiss (see above) as a former
673 allochthonous, And-bearing crustal granite intruded into upper structural levels of the
674 continental crust, and later deformed under ductile conditions. They identified a Variscan
675 high-grade assemblage in this rock because they found that the euhedral and oscillatory-zoned
676 zircon rims that are characteristic of the crystallization from a melt, such as the host anatexitic
677 granite, are Variscan in age (285 ± 5 Ma). The later development of the main metamorphic
678 foliation of the orthogneiss (formed by Qtz, Kfs, Pl, Bt, white mica and rare fibrolite) was
679 assigned by these authors to the Alpine tectono-metamorphic reworking. Zeck and
680 Whitehouse (2002) studied zircons in the schist tectonically overlying the Torrox gneiss. They
681 attributed relict And and St wrapped by the main schistosity to the Variscan orogeny, based
682 on Variscan zircon ages (313 ± 7 Ma) obtained from domains with subtle oscillatory zoning.
683 This oscillatory zoning was interpreted to have formed during Oswald ripening and growth of
684 new large metamorphic zircons from minuscule clastic zircon grains present in the
685 sedimentary parent material. Minerals forming the main schistosity of the rock (Bt, white
686 mica, Qtz, Pl, Gr) was suggested to be of Alpine age because the foliation in the basement and
687 the post-Variscan covers in this area are parallel. A similar conclusion was reached for the
688 graphite schist investigated by Zeck and Williams (2001), in which Variscan medium-grade
689 metamorphism was dated by zircon sector zoned euhedral cores (305 ± 3 Ma), while the ~ 20
690 Ma were related to the Alpine orogeny. We notice that in the case of the studied migmatites at
691 Istán, however, all high-temperature fabrics present in these rocks must be pre-Variscan
692 and/or Variscan, as they were either obliterated (foliation in the orthogneiss) or produced
693 (magmatic foliation in diatexites) during the Variscan anatexis. Thus, we have identified a
694 previously unknown Variscan domain within the Betic Cordillera that has not re-equilibrated

695 in terms of mineral assemblages and high-temperature tectonic fabric during the Alpine
696 orogeny.

697 The studied migmatites of the Alpujarride complex represent a Variscan basement that has
698 been involved in the Alpine orogeny that produced the Betic Cordillera. This and previous
699 studies conducted in the Betic-Rif orogen indicate that basement sections have not been
700 completely overprinted. These recycled Variscan basements preserve pre-Alpine mineral
701 associations and fabrics to various degrees (Zeck and Whitehouse, 1999; Zeck and Williams,
702 2001; Rossetti et al., 2010; this work). This leads to variable re-equilibration of
703 geochronological systems including the partial resetting of U-Pb ages in zircon (Sánchez-
704 Rodríguez, 1998; this work), partial to total resetting of U-Th-Pb in monazite (e.g. Montel et
705 al., 2000; Rossetti et al., 2010), and the total resetting of K-Ar and Rb-Sr in amphiboles and
706 micas (e.g. Loomis, 1975; Zeck et al., 1989a; Monié et al., 1994; Platt et al., 2003a). Now that
707 the existence of a regional Variscan high-grade metamorphism is well established, future
708 investigations of high grade Alpujarride units should aim to identify Variscan versus Alpine
709 assemblages and refine the P-T-time paths of these separate orogenic events, as suggested by
710 Zeck and Whitehouse (2002).

711 The Variscan rocks investigated in this study are close (hundreds of meters) to the contact
712 with the overlying Ronda peridotites, thus suggesting a pre-Alpine emplacement of the mantle
713 rocks. Clear evidence of Alpine anatexis in the area is only found in leucocratic dikes within
714 the peridotite itself (Priem et al., 1979; Acosta, 1998; Sánchez-Rodríguez, 1998; Esteban et
715 al., 2011a). Based on regional arguments and a previous zircon geochronological study of
716 mylonites (strongly deformed former migmatites) located at the very contact with the
717 peridotites (Esteban et al., 2011a), previous authors have concluded that the crustal
718 emplacement of the peridotites occurred in Alpine times. In the light of our results, we
719 suggest that a detailed geochronological investigation focused on migmatites located at the

720 very contact with the Ronda peridotites is necessary to unravel the relationships between
721 Variscan migmatites and potential Alpine migmatites/mylonites.

722 **9. Concluding remarks**

723 The age of metamorphism in the crystalline basements involved in the Alpine Betic-Rif
724 orogen (S Spain and N Morocco), and in particular of the highest-grade rocks, namely felsic
725 migmatites and granulites, has been the subject of a long controversy. These highest-grade
726 rocks appear systematically associated in space with the Ronda and Beni Bousera peridotite
727 slabs. Metamorphic assemblages and fabrics in these rocks have been ascribed to the Alpine
728 orogeny, or the Variscan orogeny, or both. This uncertainty emerges from the difficulty of
729 relating zircon radiometric ages to the main metamorphic assemblages. Our study provides
730 the first (and systematic) U-Pb SHRIMP zircon ages from the migmatitic sequence of Istán
731 (Guadaiza unit, Alpujárride complex, hinterland of the Betic Cordillera), located beneath the
732 Ronda peridotites. In contrast to previous zircon U-Pb studies that dated a single high-grade
733 rock within the high-grade crustal sequence, we relate zircon growth with metamorphic
734 assemblages by dating and studying the microstructures of zircons in several samples
735 throughout the migmatitic sequence, from metatexites to diatexites. Thus, we show that
736 crustal anatexis and tectonic fabrics present in this crustal sequence are Variscan in age and,
737 hence, we have identified a previously unknown Variscan domain within the Betic Cordillera
738 that has not re-equilibrated during the Alpine orogeny. Together with previous
739 geochronological studies, this new ages indicate that basement sections in the Betic-Rif
740 orogen have not been completely overprinted during the Alpine orogeny, and preserve pre-
741 Alpine mineral assemblages and fabrics. The preservation of old mineral assemblages in the
742 basement sections of orogens is an important phenomenon because it hampers establishing
743 correct P-T-time paths and hence tectonic interpretations of the orogens, and has been
744 previously recognized in orogens world wide, including other peri-mediterranean Alpine

745 orogens (e.g. the Alps, Hermann et al., 1997). The studied rocks are close (hundreds of
746 meters) to the contact with the Ronda peridotites, thus suggesting a pre-Alpine emplacement
747 of the mantle rocks. Nevertheless, based on regional arguments and a previous zircon
748 geochronological study of migmatites/mylonites located at the very contact with the
749 peridotites, previous authors have concluded that the crustal emplacement of the peridotites
750 occurred in Alpine times. In the light of our results, we suggest that a detailed
751 geochronological investigation focused on migmatites located at the very contact with the
752 Ronda peridotites is necessary to unravel the relationships between Variscan migmatites and
753 the potential Alpine migmatites/mylonites.

754 **Acknowledgements**

755 This work was supported by the Ministerio de Ciencia e Innovación of Spain (Ramón y
756 Cajal research contract to A.A.V. and grants CGL2007-62992, CTM2005-08071-C03-01,
757 CSD2006-0041, AMB93-0535, AMB94-1420, PB96-1266), the Italian Ministry of Education,
758 University and Research (grant PRIN 2010TT22SC), and the University of Padua (Progetto di
759 Ateneo CPDA107188/10. A.A.V. thanks Fernando Bea and Francisco González-Lodeiro for
760 discussion during field work. We thank Dr. G.B. Morgan for conducting the electron
761 microprobe analyses, Prof. Eby for the editorial handling, and Drs. Zeck and Fernández-
762 Suarez whose reviews improved the clarity of this manuscript.

763

764 **References**

- 765 Acosta, A., 1998. Estudio de los fenómenos de fusión cortical y generación de granitoides
766 asociados a las peridotitas de Ronda. Unpublished PhD Thesis, Universidad de Granada,
767 p. 305.
- 768 Acosta-Vigil, A., Pereira, M.D., Shaw, D.M., London, D., 2001. Contrasting behaviour of B
769 during crustal anatexis. *Lithos* 56, 15–31.
- 770 Acosta-Vigil, A., London, D., Morgan VI, G.B., Dewers, T.A., 2003. Solubility of excess
771 alumina in hydrous granitic melts in equilibrium with peraluminous minerals at 700-
772 800°C and 200 MPa, and applications of the aluminum saturation index. *Contributions*
773 *to Mineralogy and Petrology* 146, 100–119.
- 774 Acosta-Vigil, A., Buick, I., Hermann, J., Cesare, B., Rubatto, D., London, D., Morgan VI,

775 G.B., 2010. Mechanisms of crustal anatexis: a geochemical study of partially melted
776 metapelitic enclaves and host dacite, SE Spain. *Journal of Petrology* 51, 785–821.

777 Alpert, L.A., Miller, M.S., Becker, T.W., Allam, A.A., 2013. Structure beneath the Alboran
778 from geodynamic flow models and seismic anisotropy. *Journal of Geophysical Research*
779 *Solid Earth* 118, 4265–4277.

780 Andriessen, P.A.M., Zeck, H.P., 1996. Fission-track constraints on timing of Alpine nappe
781 emplacement and rates of cooling and exhumation, Torrox area, Betic Cordilleras, S.
782 Spain. *Chemical Geology* 131, 199–206.

783 Andrieux et al., 1971 Andrieux, J., Fontbote, J. M., Mattauer, M., 1971. Sur un modèle
784 explicatif de l'arc de Gibraltar. *Earth and Planetary Science Letters* 12, 191–198.

785 Argles, T.W., Platt, J.P., Waters, D.J., 1999. Attenuation and excision of a crustal section
786 during extensional exhumation: the Carratraca Massif, Betic Cordillera, southern Spain.
787 *Journal of the Geological Society of London* 156, 149–162.

788 Azañón, J.M., Crespo-Blanc, A., García-Dueñas, V., 1997. Continental collision, crustal
789 thinning and nappe forming during the pre-Miocene evolution of the Alpujarride
790 Complex (Alborán Domain, Betics). *Journal of Structural Geology* 19, 1055–1071.

791 Balanyá, J.C., García-Dueñas, V., 1987. Les directions structurales dans le Domaine
792 d'Alborán de part et d'autre du Déroit de Gibraltar. *Comptes Rendus de l'Académie*
793 *des Sciences Paris* 304, 929–932.

794 Balanyá, J.C., García-Dueñas, V., Azañón, J.M., Sánchez-Gómez, M., 1997. Alternating
795 contractional and extensional events in the Alpujarride nappes of the Alborán Domain
796 (Betics, Gibraltar arc). *Tectonics* 16, 226–238.

797 Bartoli O., Tajmanová, L., Cesare B., Acosta-Vigil, A., 2013. Phase equilibria constraints on
798 melting of stromatic migmatites from Ronda (S Spain): insights on peritectic garnet
799 formation. *Journal of Metamorphic Geology* 31, 775–789.

800 Blanco, M.J., Spakman, W., 1993. The P-wave velocity structure of the mantle below the
801 Iberian Peninsula: evidence for subducted lithosphere below southern Spain.
802 *Tectonophysics* 221, 13–34.

803 Black, L.P., Kamo, S.L., Allen, C.M., Aleinikoff, J.M., Davis, D.W., Korsch, R.J., Foudoulis,
804 C., 2003. TEMORA 1: a new zircon standard for Phanerozoic U-Pb geochronology.
805 *Chemical Geology* 200, 155–170.

806 Blumenthal, M., 1930. Beiträge zur Geologie der Betischen Cordilleren beiderseits des Río
807 Guadalhorce. *Eclogae Geologicae Helvetiae* 23, 41-293.

- 808 Bouybaouène, M.L., Michard, A., Goffé, B., 1998. High-pressure granulites on top of the
809 Beni Bousera peridotites, Rif Belt, Morocco: a record of an ancient thickened crust in
810 the Alborán domain. *Bulletin de la Société Géologique de France* 2, 153–162.
- 811 Brown, M., 2008. Granites, migmatites and residual granulites: relationships and processes. In
812 Sawyer, E.W., Brown, M. (Eds.), *Working with Migmatites*. Mineralogical Association
813 of Canada, Short Course 38, 97–144.
- 814 Brown, M., 2013. Granite: from genesis to emplacement. *Bulletin of the Geological Society*
815 of America 125, 1079–1113.
- 816 Brown, M.A., Brown, M., Carlson, W.D., Denison, C., 1999. Topology of syntectonic melt
817 flow networks in the deep crust: inferences from three-dimensional images of
818 leucosome geometry in migmatites. *American Mineralogist* 84, 1793–1818.
- 819 Butera, K.M., Williams, I.S., Blevin, P.L., Simpson, C.J., 2004. Zircon U-Pb dating of early
820 paleozoic monzonitic intrusives from the Goonumbla area, New South Wales.
821 *Australian Journal of Earth Sciences* 48, 457–464.
- 822 Cesare, B., Acosta-Vigil A., Ferrero, S., Bartoli O., 2011. Melt inclusions in migmatites and
823 granulites. In: Forster, M.A., Fitz Gerald, J.D. (Eds.), *The Science of Microstructure –*
824 *Part II*. *Journal of the Virtual Explorer, Electronic Edition*, ISSN 1441-8142, 38, paper 2.
- 825 Cesare, B., Gómez-Pugnaire, M.T., Rubatto, D., 2003. Residence time of S-type anatectic
826 magmas beneath the Neogene Volcanic Province of SE Spain: a zircon and monazite
827 SHRIMP study. *Contributions to Mineralogy and Petrology* 146, 28–43.
- 828 Cesare, B., Rubatto, D., Gómez-Pugnaire, M.T., 2009. Do extrusion ages reflect magma
829 generation processes at depth? An example from the Neogene Volcanic Province of SE
830 Spain. *Contributions to Mineralogy and Petrology* 157, 267–279.
- 831 Coggon, R., Holland, T. J. B., 2002. Mixing properties of phengitic micas and revised garnet–
832 phengite thermobarometers. *Journal of Metamorphic Geology* 20, 683–696.
- 833 Comas, M.C., Platt, J.P., Soto, J.I., Watts, A.B., 1999. The origin and tectonic history of the
834 Alborán basin: insight from ODP leg 161 results, in: Zahn, R., Comas, M.C., Klaus, A.
835 (Eds.). *Proceedings of the Ocean Drilling Program Scientific Results* 161, 555–580.
- 836 Connolly, J.A.D., 2009. The geodynamic equation of state: what and how. *Geochemistry*
837 *Geophysics Geosystems* 10, Q10014.
- 838 Ebadi, A., Johannes, W., 1991. Beginning of melting and composition of first melts in the
839 system Qz-Ab-Or-H₂O-CO₂. *Contributions to Mineralogy and Petrology* 106, 286–295.
- 840 Egeler, C.G., Simons, O.J., 1969. Sur la tectonique de la zone Bétique (Cordillères Bétiques,
841 Espagne). *Verh. Kon. Ned. Akad. Wetensch. Afd. Natuurk.* 25, 1–90.

- 842 Esteban, J.J., Cuevas, J., Vegas, N., Tubía, J.M., 2008. Deformation and kinematics in a melt-
843 bearing shear zone from the western Betic Cordilleras (southern Spain). *Journal of*
844 *Structural Geology* 30, 380–393.
- 845 Esteban, J.J., Cuevas, J., Tubía, J.M., Sergeev, S., Larionov, A., 2011a. A revised Aquitanian
846 age for the emplacement of the Ronda peridotites (Betic Cordilleras, southern Spain).
847 *Geological Magazine* 148, 183–187.
- 848 Esteban, J.J., Tubía, J.M., Cuevas, J., Vegas, N., Sergeev, S., Larionov, A., 2011b. Peri-
849 Gondwanan provenance of pre-Triassic metamorphic sequences in the western
850 Alpujarride nappes (Betic Cordillera, southern Spain). *Gondwana Research* 20, 443–
851 449.
- 852 Fernández-Suárez, J., Corfu, F., Arenas, R., Marcos, A., Martínez Catalán, J.R., Díaz García,
853 F., Abati, J, Fernández, F.J., 2002. U-Pb evidence for a polyorogenic evolution of the
854 HP-HT units of the NW Iberian Massif. *Contributions to Mineralogy and Petrology*
855 143, 236–253.
- 856 Foucault, A., Paquet, J., 1971. Sur l'importance d'une tectogénèse hercynienne dans la région
857 centrale des Cordillères bétiques. *Comptes Rendus de l'Académie des Sciences Paris*
858 272, 2756–2758.
- 859 García-Casco, A., Torres-Roldán, R.L., 1996. Disequilibrium induced by fast decompression
860 in St-Bt-Grt-Ky-Sil-And metapelites from the Betic Belt (southern Spain). *Journal of*
861 *Petrology* 37, 1207–1239.
- 862 Goffé, B., Michard, A., García-Dueñas, V., González-Lodeiro, F., Monié, P., Campos, J.,
863 Galindo-Zaldívar, J., Jabaloy, A., Martínez-Martínez, J.M., Simancas, F., 1989. First
864 evidence of high-pressure, low-temperature metamorphism in the Alpujarride nappes,
865 Betic Cordilleras (SE Spain). *European Journal of Mineralogy* 1, 139–142.
- 866 Galindo-Zaldívar, J., González-Lodeiro, F., Jabaloy, A., Maldonado, A., Schreider, A., 1998.
867 Models of magnetic and Bouguer gravity anomalies for the deep structure of the central
868 Alboran Sea basin. *Geo-Marine Letters* 18, 10–18.
- 869 Harley, S.L, Kelly, N.M., 2007. The impact of zircon–garnet REE distribution data on the
870 interpretation of zircon U–Pb ages in complex high-grade terrains: an example from the
871 Rauer Islands, East Antarctica. *Chemical Geology* 241, 62–87.
- 872 Hermann, J., Rubatto, D., 2003. Relating zircon and monazite domains to garnet growth
873 zones: age and duration of granulite facies metamorphism in the Val Malenco lower
874 crust. *Journal of Metamorphic Geology* 21, 833–852.

- 875 Hermann, J., Müntener, O., Trommsdorff, V., Hansmann, W., 1997. Fossil crust-to-mantle
876 transition, Val Malenco (Italian Alps). *Journal of Geophysical Research* 102, 20123–
877 20192.
- 878 Hermann, J., Rubatto, D., Trommsdorff, V., 2006. Sub-solidus Oligocene zircon formation in
879 garnet peridotite during fast decompression and fluid infiltration (Duria, Central Alps).
880 *Mineralogy and Petrology* 88, 181–206.
- 881 Hoepfner, R., Hoppe, P.H.M., Muchow, S., Dürr, S., Kockel, F., 1964. Über den westlichen
882 Abschnitt der Betischen Kordilleren und seine Beziehungen zum Gesamtorogen.
883 *Geologische Rundschau* 53, 269–296.
- 884 Holland, T. J. B., Powell, R., 1998. An internally consistent thermodynamic data set for
885 phases of petrological interest. *Journal of Metamorphic Geology* 16, 309–343.
- 886 Holland, T. J. B., Powell, R., 2003. Activity-composition relations for phases in
887 petrological calculations: an asymmetric multicomponent formulation.
888 *Contributions to Mineralogy and Petrology* 145, 492–501.
- 889 Holland, T.J.B., Powell, R., 2001. Calculation of phase relations involving haplogranitic melts
890 using an internally consistent thermodynamic data set. *Journal of Petrology* 42, 673–
891 683.
- 892 Janots, E., Negro, F., Brunet, F., Goffé, B., Engi, M., Bouybaouène, M.L., 2006. Evolution of
893 the REE mineralogy in HP-LT metapelites of the Sebti complex, Rif, Morocco:
894 monazite stability and geochronology. *Lithos* 87, 214–234.
- 895 Janots, E., Engi, M., Rubatto, D., Berger, A., Gregory, C., Rahn, M., 2009. Metamorphic rates
896 in collisional orogeny from in situ allanite and monazite dating. *Geology* 37, 11–14.
- 897 Kretz, R., 1983. Symbols for rock-forming minerals. *American Mineralogist* 68, 277–279.
- 898 Loomis, T.P., 1975. Tertiary mantle diapirism, orogeny and plate tectonics East of the Strait
899 of Gibraltar. *American Journal of Science* 275, 1–30.
- 900 López Sánchez-Vizcaíno, V., Rubatto, D., Gómez-Pugnaire, M.T., Trommsdorff, V.,
901 Müntener, O., 2001. Middle Miocene high-pressure metamorphism and fast exhumation
902 of the Nevado-Filábride Complex, SE Spain. *Terra Nova* 13, 327–332.
- 903 Ludwig, K.R., 2003. Isoplot/Ex version 3.0. A geochronological toolkit for Microsoft Excel.
904 Berkeley Geochronological Centre Special Publication 1a.
- 905 Lundeen, M.T., 1978. Emplacement of the Ronda peridotite, Sierra Bermeja, Spain.
906 *Geological Society of American Bulletin* 89, 172–180.
- 907 Luth, W.C., Jahns, R.H., Tuttle, O.F., 1964. The granite system at pressures of 4 to 10
908 kilobars. *Journal of Geophysical Research* 69, 759–773.

- 909 Martin, J.M., Braga, J.C., 1987. Alpujárride carbonate deposits (Southern Spain) - marine
910 sedimentation in a Triassic Atlantic. *Palaeogeography Palaeoclimatology* 59, 243–260.
- 911 Martín-Algarra, A., 1987. Evolución geológica alpina del contacto entre las Zonas Internas y
912 las Zonas Externas de la Cordillera Bética. PhD Thesis, Universidad de Granada, p.
913 1171.
- 914 Martín-Algarra, A., Messina, A., Perrone, V., Russo, S., Maate, A., Martín-Martín, M., 2000.
915 A lost realm in the internal domains of the Betic-Rifian orogen (Spain and Morocco):
916 evidence from Oligo-Aquitania conglomerates and consequences for alpine
917 geodynamic evolution. *Journal of Geology* 108, 447–467.
- 918 Martín-Algarra, A., Mazzoli, S., Perrone, V., Rodríguez-Cañero, R., Navas-Parejo, P., 2009.
919 Variscan tectonics in the Maláguide Complex (Betic Cordillera, Southern Spain):
920 stratigraphic and structural Alpine versus pre-Alpine constraints from the Ardales area
921 (Province of Málaga). I. Stratigraphy. *Journal of Geology* 117, 241–262.
- 922 Mazzoli, S., Martín-Algarra, A., 2011. Deformation partitioning during transpressional
923 emplacement of a 'mantle extrusion wedge': the Ronda peridotites, western Betic
924 Cordillera, Spain. *Journal of the Geological Society of London* 168, 373–382.
- 925 Michard, A., Goffé, B., Bouybaouene, M.L., Saddiqi, O., 1997. Late Hercynian–Mesozoic
926 thinning in the Alboran domain: metamorphic data from the northern Rif, Morocco.
927 *Terra Nova* 9, 171–174.
- 928 Michard, A., Negro, F., Saddiqi, O., Bouybaouene, M.L., Chalouan, A., Montigny, R., Goffé,
929 B., 2006. Pressure-temperature-time constraints on the Maghrebide mountain building:
930 evidence from the Rif-Betic transect (Morocco, Spain), Algerian correlations, and
931 geodynamic implications. *Comptes Rendus de l'Académie des Sciences Paris* 338, 92–
932 114.
- 933 Mollat, H., 1968. Schichtenfolge und tektonischer Bau der Sierra Blanca und ihrer Umgebung
934 (Betische Kordilleren, Südsanien). *Geologisches Jahrbuch* 86, 471–532.
- 935 Monié, P., Galindo-Zaldívar, J., González Lodeiro, F., Goffé, B., Jabaloy, A., 1991. $^{40}\text{Ar}/^{39}\text{Ar}$
936 geochronology of Alpine tectonism in the Betic Cordilleras (southern Spain). *Journal of*
937 *the Geological Society of London* 148, 289–297.
- 938 Monié, P., Torres-Roldán, R.L., García-Casco, A., 1994. Cooling and exhumation of the
939 Western Betic Cordilleras, $^{40}\text{Ar}/^{39}\text{Ar}$ thermochronological constraints on a collapsed
940 terrane. *Tectonophysics* 238, 353–379.

- 941 Montel, J.M., Kornprobst, J., Vielzeuf, D., 2000. Preservation of old U–Th–Pb ages in
942 shielded monazite: example from the Beni Bousera Hercynian kinzigites (Morocco).
943 *Journal of Metamorphic Geology* 18, 335–342.
- 944 Navarro-Vilá, F., Tubía, J.M., 1983. Essai d’une nouvelle différenciation des Nappes
945 Alpujarrides dans le secteur occidental des Cordillères Bétiques (Andalousie, Espagne).
946 *Comptes Rendus de l’Académie des Sciences Paris* 296, 111–114.
- 947 Newton, R.C., Charlu, T.V., Kleppa, O.J., 1980. Thermochemistry of high structural state
948 plagioclases. *Geochimica et Cosmochimica Acta* 44, 933–941.
- 949 Obata, M., 1980. The Ronda peridotite: Garnet-, Spinel-, and Plagioclase-Lherzolite facies
950 and the P-T trajectories of high temperature mantle emplacement. *Journal of Petrology*
951 21, 533–572.
- 952 Patiño Douce, A.E., Harris, N., 1998. Experimental constraints on Himalayan anatexis.
953 *Journal of Petrology* 39, 689–710.
- 954 Pedrera, A., Ruiz-Constán, A., Galindo-Zaldívar, J., Chalouan, A., Sanz de Galdeano, C.,
955 Marín-Lechado, C., Ruano, P., Benmakhlouf, M., Akil, M., López Garrido, A.C.,
956 Chabli, A., Ahmamou, M., González-Castillo, L., 2011. Is there an active subduction
957 beneath the Gibraltar orogenic arc? Constraints from Pliocene to present-day stress field.
958 *Journal of Geodynamics* 52, 83–96.
- 959 Pidgeon, R.T., Nemchin, A.A., Hitchen, G.J., 1998. Internal structures of zircons from
960 Archean granites from the Darling Range batholith: implications for zircon stability and
961 the interpretation of zircon U-Pb ages. *Contributions to Mineralogy and Petrology* 132,
962 288–299.
- 963 Piles, E., Chamón, C., Estévez-González, C., 1978. Mapa y memoria explicativa de la hoja
964 1065 (Marbella) del Mapa Geológico Nacional a escala 1:50.000. Instituto Geológico y
965 Minero de España.
- 966 Platt, J.P., Whitehouse, M.J., 1999. Early Miocene high-temperature metamorphism and rapid
967 exhumation in the Betic Cordillera (Spain): evidence from U-Pb zircon ages. *Earth and*
968 *Planetary Science Letters* 171, 591–605.
- 969 Platt, J.P., Soto, J.I., Whitehouse, M.J., Hurford, A.J., Kelley, S.P., 1998. Thermal evolution,
970 rate of exhumation, and tectonic significance of metamorphic rocks from the floor of the
971 Alborán extensional basin, western Mediterranean. *Tectonics* 17, 671–689.
- 972 Platt, J.P., Argles, T.W., Carter, A., Kelley, S.P., Whitehouse, M.J., Lonergan, L., 2003a.
973 Exhumation of the Ronda peridotite and its crustal envelope: constraints from thermal

- 974 modelling of a P–T–time array. *Journal of the Geological Society of London* 160, 655–
975 676.
- 976 Platt, J.P., Whitehouse, M.J., Kelley, S.P., Carter, A., Hollick, L., 2003b. Simultaneous
977 extensional exhumation across the Alborán Sea: implications for the causes of late
978 orogenic extension. *Geology* 31, 251–254.
- 979 Platt, J.P., Kelley, S.P., Carter, A., Orozco, M., 2005. Timing of tectonic events in the
980 Alpujarride Complex, Betic Cordillera, southern Spain. *Journal of the Geological*
981 *Society of London* 162, 451–462.
- 982 Platt, J.P., Anczkiewicz, R., Soto, J.I., Kelley, S.P., Thirlwall, M., 2006. Early Miocene
983 continental subduction and rapid exhumation in the western Mediterranean. *Geology* 34,
984 981–984.
- 985 Platt, J.P., Behr, W.M., Johannesen, K., Williams, J.R., 2013. The Betic-Rif arc and its
986 orogenic hinterland: a review. *Annual Review of Earth and Planetary Sciences* 41,
987 14.1–14.45.
- 988 Pouchou, J.L., Pichoir, F., 1985. $\rho(\phi z)$ correction procedure for improved quantitative
989 microanalysis. In: Armstrong, J.T. (Ed.), *Microbeam analysis*. San Francisco Press, San
990 Francisco, pp 104–106.
- 991 Priem, H. N. A., Boelrijk, N. A. I. M., Hebeda, E. H., Oen, I. S., Verdurmen, E. A. Th.,
992 Verschure, R. H., 1979. Isotopic dating of the emplacement of the ultramafic masses in
993 the Serranía de Ronda, Southern Spain. *Contributions to Mineralogy and Petrology* 70,
994 103–109.
- 995 Rossetti, F., Theye, T., Lucci, F., Bouybaouene, M.L., Dini, A., Gerdes, A., Phillips, D.,
996 Cozzupoli, D., 2010. Timing and modes of granite magmatism in the core of the
997 Alborán Domain, Rif chain, northern Morocco: implications for the Alpine evolution of
998 the western Mediterranean. *Tectonics* 29, doi: 10.1029/2009TC002487.
- 999 Rubatto, D., 2002. Zircon trace element geochemistry: partitioning with garnet and the link
1000 between U-Pb ages and metamorphism. *Chemical Geology* 184, 123–138.
- 1001 Rubatto, D., Chakraborty, S., Dasgupta, S., 2013. Timescales of crustal melting in the Higher
1002 Himalayan Crystallines (Sikkim, Eastern Himalaya) inferred from trace element-
1003 constrained monazite and zircon chronology. *Contributions to Mineralogy and Petrology*
1004 165, 349–372.
- 1005 Rubatto, D., Williams, I.S., Buick, I.S., 2001. Zircon and monazite response to prograde
1006 metamorphism in the Reynolds Range, central Australia. *Contributions to Mineralogy*
1007 *and Petrology* 140, 458–468.

- 1008 Sánchez-Rodríguez, L., 1998. Pre-Alpine and Alpine evolution of the Ronda Ultramafic
1009 Complex and its country-rocks (Betic chain, southern Spain): U-Pb SHRIMP zircon and
1010 fission-track dating. PhD Thesis, ETH Zürich, p. 170.
- 1011 Sánchez-Rodríguez, L., Gebauer, D., 2000. Mesozoic formation of pyroxenites and gabbros in
1012 the Ronda area (southern Spain), followed by Early Miocene subduction metamorphism
1013 and emplacement into the middle crust: U-Pb sensitive high-resolution ion microprobe
1014 dating of zircon. *Tectonophysics* 316, 19–44.
- 1015 Sanz de Galdeano, C., 1990. Geologic evolution of the Betic Cordilleras in the Western
1016 Mediterranean, Miocene to present. *Tectonophysics* 172, 107–119.
- 1017 Sanz de Galdeano, C., Andreo, B., 1995. Structure of Sierra Blanca (Alpujárride complex,
1018 west of the Betic Cordillera). *Estudios Geológicos* 51, 43–55.
- 1019 Sawyer, E.W., 2001. Melt segregation in the continental crust: distribution and movement of
1020 melt in anatectic rocks. *Journal of Metamorphic Geology* 19, 291–309.
- 1021 Sawyer, E.W., 2008. Atlas of Migmatites. The Canadian Mineralogist Special Publication 9,
1022 NRC Research Press, Ottawa, Ontario, Canada.
- 1023 Sawyer, E.W., 2010. Migmatites formed by water-fluxed partial melting of a
1024 leucogranodiorite protolith: microstructures in the residual rocks and source of the fluid.
1025 *Lithos* 116, 273–286.
- 1026 Simancas, J.F., Campos, J., 1993. Compresión NNW-SSE tardi a postmetamórfica y
1027 extensión subordinada en el Complejo Alpujárride (Dominio de Alborán Orógeno
1028 Bético). *Revista de la Sociedad Geológica de España* 6, 23–36.
- 1029 Sosson, M., Morillon, A.C., Bourgois, J., Féraud, G., Poupeau, G., Saint-Marc, P., 1998. Late
1030 exhumation stages of the Alpujárride Complex (western Betic Cordilleras, Spain): new
1031 thermochronological and structural data on Los Reales and Ojén nappes.
1032 *Tectonophysics* 285, 253–273.
- 1033 Stacey, J.S., Kramers, J.D., 1975. Approximation of terrestrial lead evolution by a two-stage
1034 model. *Earth and Planetary Science Letters* 26, 207–221.
- 1035 Stepanov, A.S., Hermann, J., Rubatto, D., Rapp, R.P., 2012. Experimental study of
1036 monazite/melt partitioning with implications for the REE, Th and U geochemistry of
1037 crustal melts. *Chemical Geology* 300–301, 200–220.
- 1038 Tajčmanová, L., Conolly, J.A.D., Cesare, B. 2009. A thermodynamic model for titanium and
1039 ferric iron solution in biotite. *Journal of Metamorphic Geology* 27, 153–165.

- 1040 Thompson, A.B., Algor, J.R., 1977. Model systems for anatexis of pelitic rocks. I. Theory of
1041 melting reactions in the system $\text{KAlO}_2\text{-NaAlO}_2\text{-Al}_2\text{O}_3\text{-SiO}_2\text{-H}_2\text{O}$. Contributions to
1042 Mineralogy and Petrology 63, 247–269.
- 1043 Thompson, J.B., Hovis, G.L., 1979. Entropy of mixing in sanidine. American Mineralogist
1044 64, 57–65.
- 1045 Torres-Roldán, R.L., 1981. Plurifacial metamorphic evolution of the Sierra Bermeja peridotite
1046 aureole (southern Spain). Estudios Geológicos 37, 115–133.
- 1047 Torres-Roldán, R.L., 1983. Fractionated melting of metapelite and further crystal-melt
1048 equilibria. The example of the Blanca Unit migmatite complex, north of Estepona
1049 (southern Spain). Tectonophysics 96, 95–123.
- 1050 Tubía, J.M., 1988. Estructura de los Alpujárrides occidentales: Cinemática y condiciones de
1051 emplazamiento de las peridotitas de Ronda. Publicaciones Especiales del Boletín
1052 Geológico y Minero de España 99, p. 124.
- 1053 Tubía, J.M., Gil-Ibarguchi, J.I., 1991. Eclogites of the Ojén nappe: a record of subduction in
1054 the Alpujárride complex (Betic Cordilleras, southern Spain). Journal of the Geological
1055 Society of London 148, 801–804.
- 1056 Tubía, J.M., Cuevas, J., Gil-Ibarguchi, J.I., 1997. Sequential development of the metamorphic
1057 aureole beneath the Ronda peridotites and its bearing on the tectonic evolution of the
1058 Betic Cordillera. Tectonophysics 279, 227–252.
- 1059 Tubía, J.M., Cuevas, J., Esteban, J.J., 2013. Localization of deformation and kinematics shift
1060 during the hot emplacement of the Ronda peridotites (Betic Cordilleras, southern
1061 Spain). Journal of Structural Geology 50, 148–160.
- 1062 Vernon, R.H., 2011. Microstructures of melt-bearing regional metamorphic rocks. In: Van
1063 Reenen, D.D., Kramers, J.D., McCourt, S., Perchuk, L.L. (Eds.), Origin and Evolution of
1064 Precambrian High-Grade Gneiss Terranes, with Special Emphasis on the Limpopo
1065 Complex of Southern Africa. Geological Society of America Memoir 207, 1–11.
- 1066 Watson, E.B., Harrison, T.M., 1983. Zircon saturation revisited: temperature and composition
1067 effects in a variety of crustal magma types. Earth and Planetary Science Letters 64, 295–
1068 304.
- 1069 Westerhof, A.B., 1977. On the contact relations of high-temperature peridotites in the
1070 Serranía de Ronda, southern Spain. Tectonophysics 39, 579–591.
- 1071 White R.W., Powell R., Holland T.J.B., 2007. Progress relating to calculation of partial
1072 melting equilibria for metapelites. Journal of Metamorphic Geology 25, 511–527.

- 1073 Whitehouse, M.J., Platt, J.P., 2003. Dating high-grade metamorphism—constraints from rare-
1074 earth elements in zircon and garnet. *Contributions to Mineralogy and Petrology* 145,
1075 61–74.
- 1076 Williams, I. S., 1998. U-Th-Pb geochronology by ion microprobe, in: McKibben, M. A.,
1077 Shanks III, W. C., Ridley, W. I. (Eds.), *Application of Microanalytical Techniques to*
1078 *Understanding Mineralizing Processes*. *Rev. Econ. Geol.*, Society of Economic
1079 Geologists 7, p. 1-35.
- 1080 Williams, I.S., 2001. Response of detrital zircon and monazite, and their U-Pb isotopic
1081 systems, to regional metamorphism and host-rock partial melting, Cooma Complex,
1082 southeastern Australia. *Australian Journal of Earth Sciences* 48, 557–580.
- 1083 Williams, M.L., Jercinovic, M.J., 2012. Tectonic interpretation of metamorphic tectonites:
1084 intergrating compositional mapping, microstructural analysis and *in situ* monazite
1085 dating. *Journal of Metamorphic Geology* 30, 739–752.
- 1086 Zeck, H.P., Whitehouse, M.J., 1999. Hercynian, Pan-African, Proterozoic and Archean ion-
1087 microprobe zircon ages for a Betic-Rif core complex, Alpine belt, W Mediterranean—
1088 consequences for its P-T-t path. *Contributions to Mineralogy and Petrology* 134, 134–
1089 149.
- 1090 Zeck, H.P., Whitehouse, M.J., 2002. Repeated age resetting in zircons from Hercynian–
1091 Alpine polymetamorphic schists (Betic-Rif tectonic belt, S. Spain) —a U–Th–Pb ion
1092 microprobe study. *Chemical Geology* 182, 275–292.
- 1093 Zeck, H.P., Williams, I.S., 2001. Hercynian metamorphism in nappe core complexes of the
1094 Alpine Betic-Rif belt, western Mediterranean—a SHRIMP zircon study. *Journal of*
1095 *Petrology* 42, 1373–1385.
- 1096 Zeck, H.P., Albat, F., Hansen, B.T., Torres-Roldán, R.L., García-Casco, A., Martín-Algarra,
1097 A., 1989a. A 21 ± 2 Ma age for the termination of the ductile Alpine deformation in the
1098 internal zone of the Betic Cordilleras, south Spain. *Tectonophysics* 169, 215–220.
- 1099 Zeck, H.P., Albat, F., Hansen, B.T., Torres-Roldán, R.L., García-Casco, A., 1989b. Alpine
1100 tourmaline-bearing muscovite leucogranites, intrusion age and petrogenesis, Betic
1101 Cordilleras, SE Spain. *Neues Jahrbuch für Mineralogie Monatshefte* 11, 513–520.
- 1102 Zeck, H.P., Monié, P., Villa, I.M., Hansen, B.T., 1992. Very high rates of cooling and uplift
1103 in the Alpine belt of the Betic Cordilleras, southern Spain. *Geology* 20, 79–82.

1104 **Figure captions**

1105 **Figure 1.** (a) Geologic maps of the Betic-Rif orogen and the western Betic Cordillera
1106 (modified from Balanyá et al., 1997; including data from Martín-Algarra, 1987; Sanz de
1107 Galdeano and Andreo, 1995; Mazzoli and Martín-Algarra, 2011; Tubía et al., 2013),
1108 showing the several outcrops of the Guadaiza and Ojén units, the study area near the
1109 village of Istán, and the location of the cross-section shown in Fig. 1b. (b) Esquematic
1110 cross-section of the western Betic Cordillera across the peridotite massifs of Sierra
1111 Bermeja and Sierra Alpujata.

1112 **Figure 2.** Geologic map of the Istán area (modified from Piles et al., 1978; structural data
1113 from the Ojén unit are from Sanz de Galdeano and Andreo, 1995), and geologic cross-
1114 section based on this work. Red arrows refer to lineations defined by sillimanite that
1115 indicate a top-to the NW sense of shear.

1116 **Figure 3.** Field appearance and petrographic photomicrographs of the Istán orthogneiss
1117 (paleosome of metatextitic migmatites). (a-b) Orthogneiss showing a glandular structure
1118 and cm- to dm-scale isoclinal to tight N-vergent folds. The coin is 25 mm across. (c) S-C
1119 microstructures from a thin section perpendicular to S_p and parallel to the lineation defined
1120 by Sil observed in the field (red arrows in Fig. 2). These microstructures are mostly
1121 defined by Bt and fibrolite mats and show a top-to the NW sense of shear. Plane-polarized
1122 light (PPL). (d) Porphyroblast of Pl including oriented Sil needles (red arrow) and Bt
1123 (white arrow), and wrapped by folded aggregates of fibrolite and Bt (PPL). (e) Elongated
1124 and anhedral crystal of andalusite, parallel to the foliation and wrapped by fibrolite +
1125 biotite (PPL). (f) Subhedral microstructure in the orthogneiss. Note the subhedral feldspars
1126 (red arrows) and cusped terminations of feldspars and Qtz (white arrows). Cross-polarized
1127 light (CPL).

1128 **Figure 4.** Field appearance and petrographic photomicrographs of Grt-leucosomes in
1129 metatextitic migmatites. (a-b) Garnet-leucosome affected by a metric-scale N-vergent fold.

1130 Note that leucosomes are thicker in fold hinges. The hammers are 70 cm (a) and 35 cm (b)
1131 long. (c) Detail of the Grt-leucosome shown in Fig. 4b. Note that leucosomes are roughly
1132 parallel though slightly discordant with respect to the foliation in the paleosome. The coin
1133 is 25 mm across. (d-e) Garnets in the leucosome crowded with small ($\leq 5 \mu\text{m}$) inclusions
1134 and wrapped by oriented fibrolite mats (PPL). Garnets frequently include also crystals or
1135 polycrystalline aggregates of Qtz. The inset in (e) shows that some of the small inclusions
1136 may correspond to nanogranites, as they are polycrystalline and show negative crystal
1137 shapes. (f) Subhedral microstructure in Grt-leucosome (CPL). Red arrows show Pl.

1138 **Figure 5.** Pseudoternary Qtz-Or-Ab diagram showing the normative composition of the studied
1139 rocks. The following relevant equilibria in the metaluminous haplogranite system is also
1140 shown: 500 and 1000 MPa eutectics at $a_{\text{H}_2\text{O}} \leq 1$, cotectic lines and liquidus isotherms [data
1141 from Luth et al. (1964) and Ebadi and Johannes (1991)].

1142 **Figure 6.** Field appearance and petrographic photomicrographs of Crd-neosomes in
1143 metatexitic migmatites. (a-b) Cordierite-neosomes. Cordierite shows as either rounded and
1144 anhedral aggregates concentrated at the center of the neosome [(a) and center right of (b)],
1145 or euhedral and homogeneously distributed crystals [upper left of (b)]. This younger
1146 generation of neosomes partially obliterates the foliation in the paleosome, forming cm- to
1147 dm-sized undeformed pods. The pen is 15 cm long, and the coin is 25 mm across. (c)
1148 Cordierite intergrown with Qtz and wrapped by oriented fibrolite mats (CPL). (d)
1149 Subhedral to anhedral Grt included in large Pl of Crd-neosome (CPL). The inset (PPL)
1150 shows that this Grt is similar in microstructure to that of Grt-leucosomes (Figs. 4d-e). (e)
1151 Subhedral microstructure in Crd-neosome (CPL plus quartz accessory plate). Note the
1152 strong orientation of fibrolite mats (yellow arrow). White arrows show Pl. (f) Subhedral
1153 microstructure and cusped terminations of feldspars in Crd-neosome (CPL).

1154 **Figure. 7.** Field appearance and petrographic photomicrographs of diatexitic migmatites. (a-
1155 b) Schollen diatexitic migmatites where the foliated structure of the paleosome starts to disappear due
1156 to the increase in the proportion of Crd-neosomes. Note the development of a magmatic
1157 foliation within cm-to-dm bands, defined by elongated Crd aggregates (center bottom of b).
1158 The hammer is 29 cm long. (c-e) Diatexitic migmatites with variable proportions of Crd
1159 and Bt, having either granitic (c-d; mesocratic diatexitic migmatites) or leucogranitic (e; leucocratic
1160 diatexitic migmatites) compositions. The coin is 25 mm across. (f) Photomicrograph from the
1161 mesocratic diatexitic migmatites shown in Fig. 7c, showing an igneous subhedral microstructure. (g)
1162 Schlieric diatexitic migmatites at ≈ 100 -150 m from the contact with the peridotites, showing a cm-to-
1163 dm flow banding. The coin is 25 mm across. (h) Photomicrograph from the schlieric
1164 diatexitic migmatite shown in Fig. 6g, showing a subhedral microstructure.

1165 **Figure. 8.** Schematic evolution of the Istán migmatites with increasing time and temperature
1166 and decreasing distance with the Ronda peridotite contact. The sketch shows the
1167 relationships between all described rock types in this work. (a-b) The paleosome
1168 (orthogneiss) shows cm-to-dm Grt-bearing melt-rich bands (Grt-leucosomes) that are
1169 roughly parallel to the main foliation in the rock (S_p), and likely formed before folding of
1170 S_p . The rock is above its solidus during folding, as shown by the frequent subhedral
1171 microstructure in the paleosome and Grt-leucosomes and the thicker Grt-leucosomes in
1172 fold hinges (compare with Figs. 3a, 4a-c). (c) After folding of S_p , cm-to-dm Crd-bearing
1173 leucocratic patches (Crd-neosomes) form and locally obliterate the main foliation in the
1174 rock (compare with Figs. 6a-b). (d) With increasing time and temperature and decreasing
1175 the distance with the peridotite contact, the proportion of Crd-neosomes increases and the
1176 pre-partial melting structure of the rock starts to disappear, forming schollen diatexitic migmatites.
1177 Concomitantly, a magmatic foliation defined by elongated Crd aggregates and Kfs
1178 megacrysts, develops in cm-to-dm bands of the rock [lower part of (d), compare with Figs.

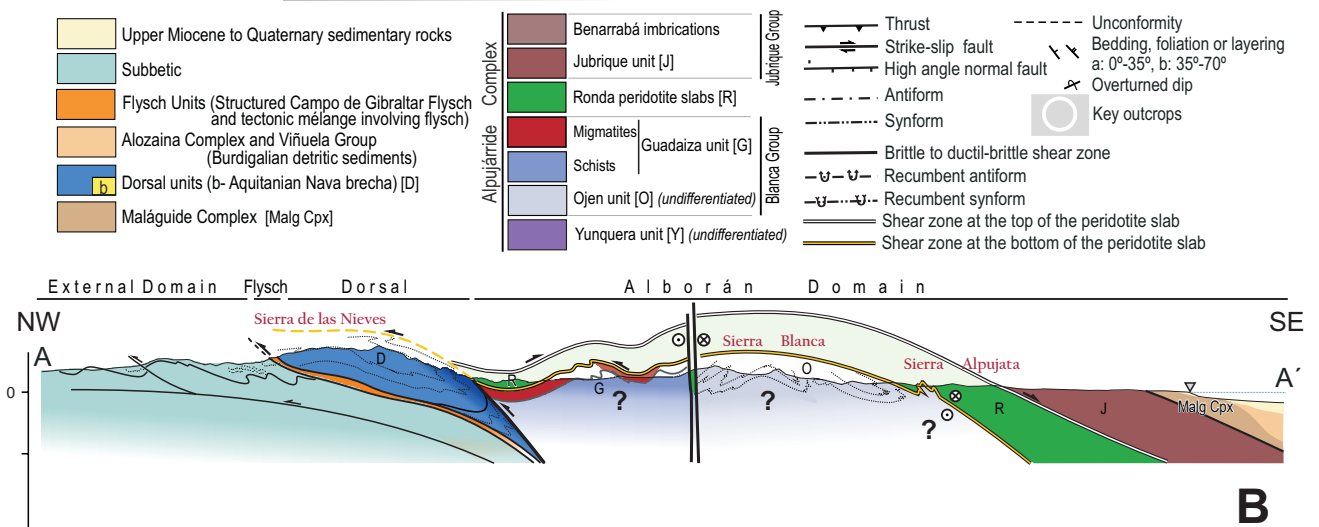
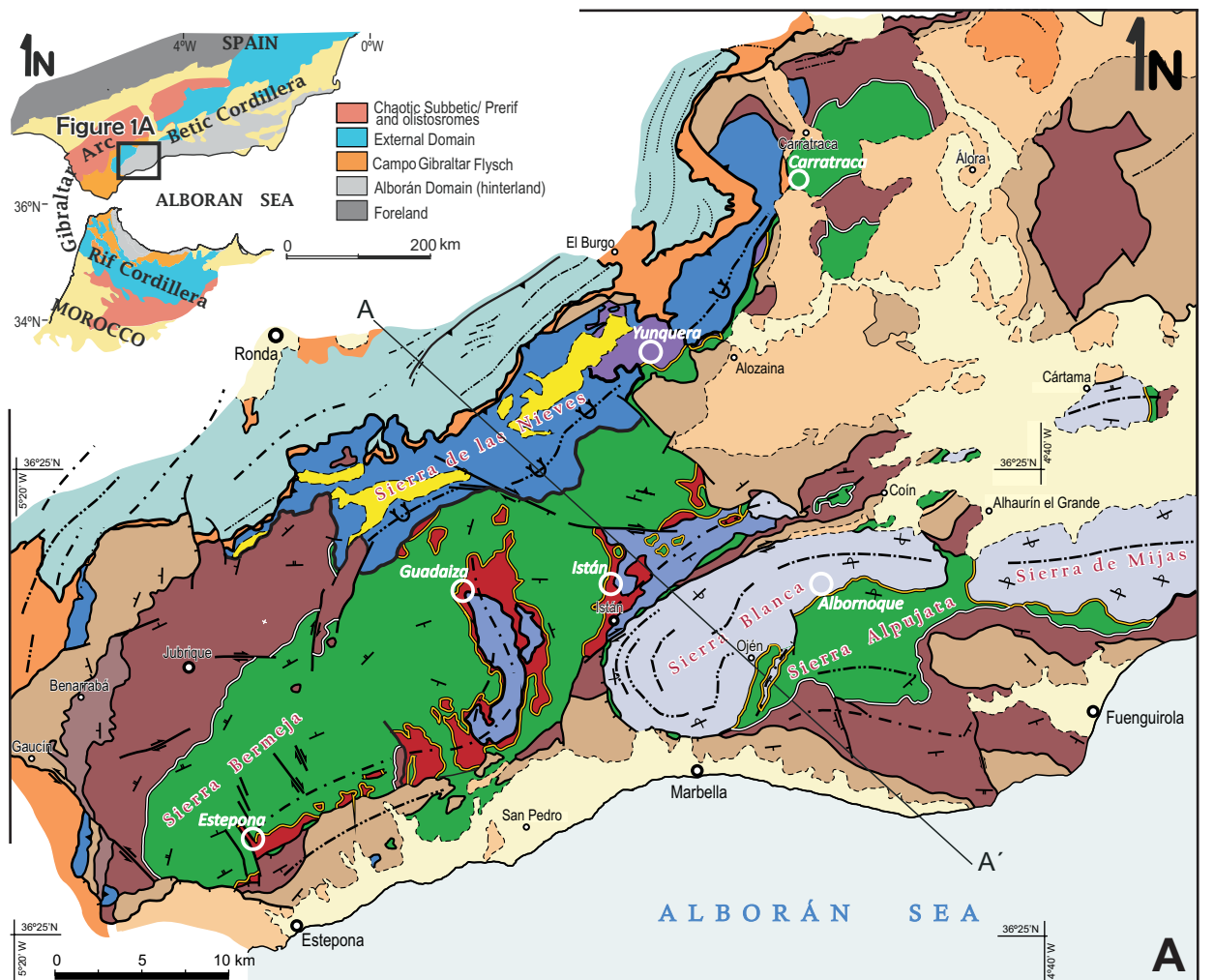
1179 7a-b]. (e) Close to the contact with the peridotites the proportion of neosome dominates
1180 volumetrically over the paleosome, and the latter is only visible as rare, small and rounded
1181 fragments included within a Crd-rich diatexite. The diatexite appears either massive
1182 (mesocratic and leucocratic diatexites) or with a flow banding (schlieric diatexite) defined
1183 by variations in the proportion of Bt and Crd (compared with Figs. 7c-d, 7e, 7g). See text
1184 for more details.

1185 **Figure. 9.** *P-T* section for the mesocratic diatexite Ista-16 calculated in the system
1186 MnNCKFMASH. It applies also to paleosome Ista-15, as both bulk rock compositions are
1187 very similar. The red arrow indicates an illustrative nearly isobaric *P-T* path, inferred based
1188 on both modeling and microstructural observations. See text for details.

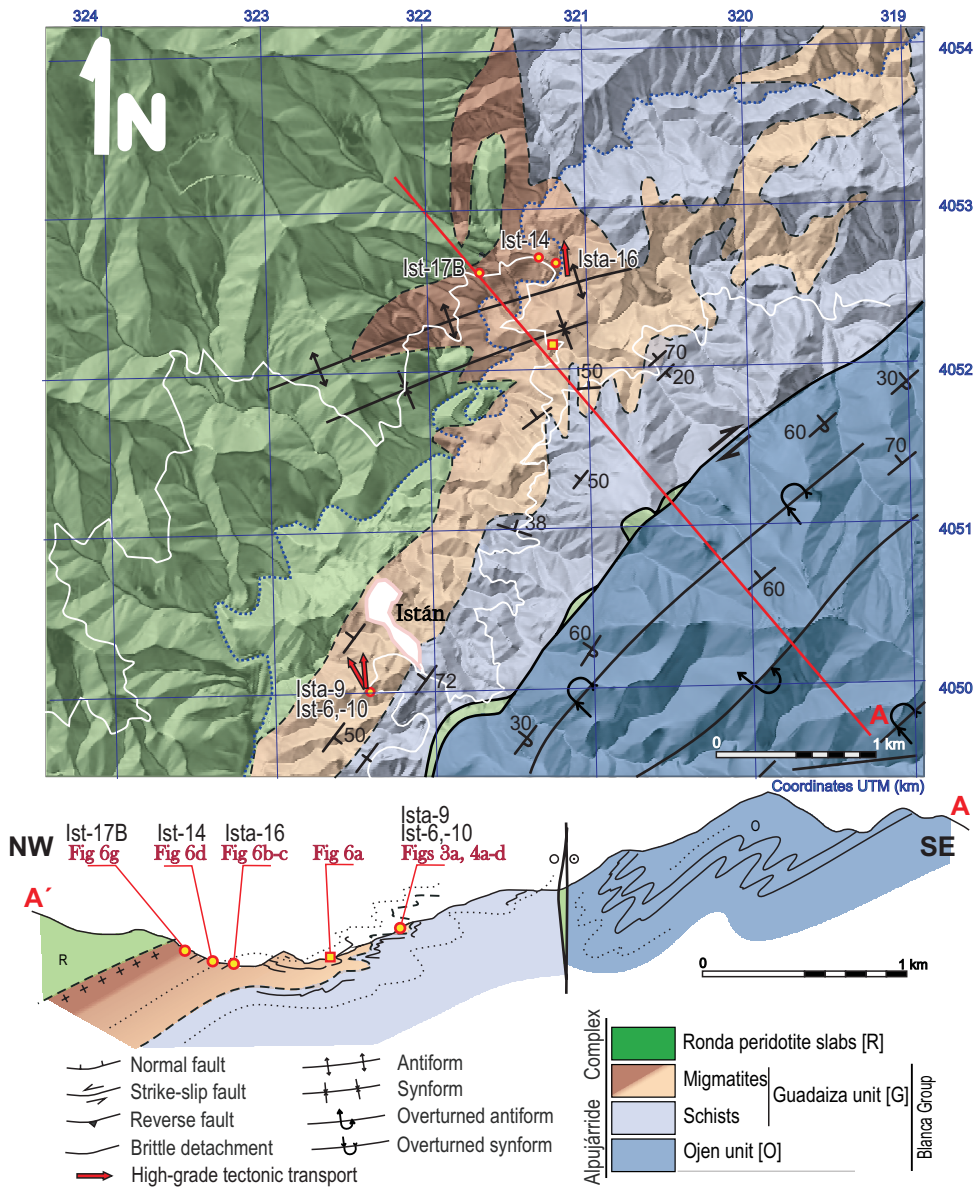
1189 **Figure. 10.** Cathodoluminescence images of representative zircon crystals. Circles indicate
1190 the location of the SHRIMP U-Pb analyses, with a diameter of $\sim 25\mu\text{m}$. The numbers
1191 beside each circle indicate the date in Ma (see Supplementary Table 1 for uncertainties).
1192 The corresponding back-scattered image is shown for crystals IST10-11, IST10-1, IST6-5
1193 and IST14-1; these images show the inclusion trails and porosity of the damaged rims. See
1194 text for details.

1195 **Figure. 11.** (a-f) Concordia diagrams for U-Pb SHRIMP analyses of zircon domains. Ellipses
1196 represent 2σ errors. (g) Cumulative probability density plots for SHRIMP U-Pb dates.

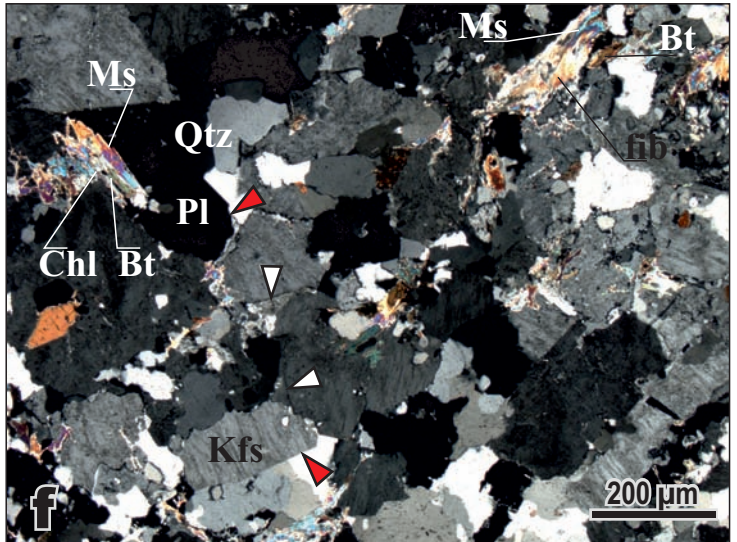
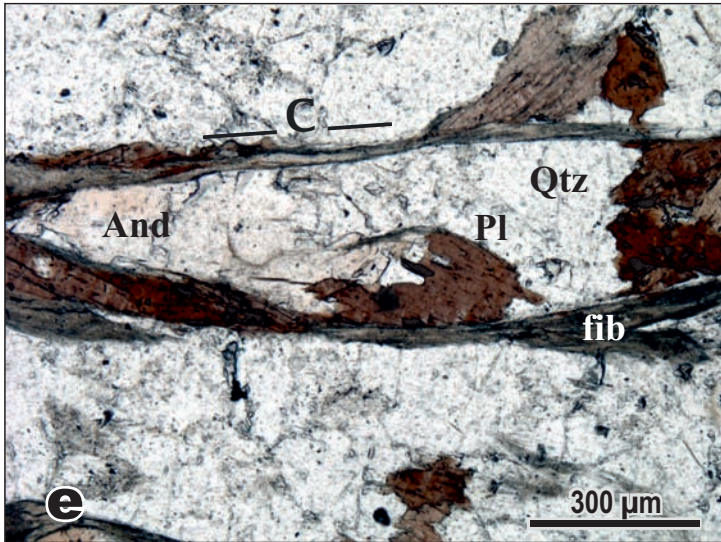
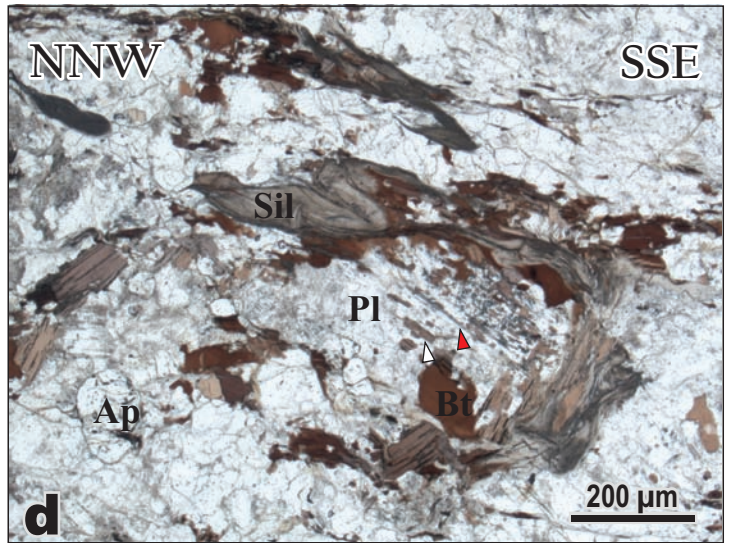
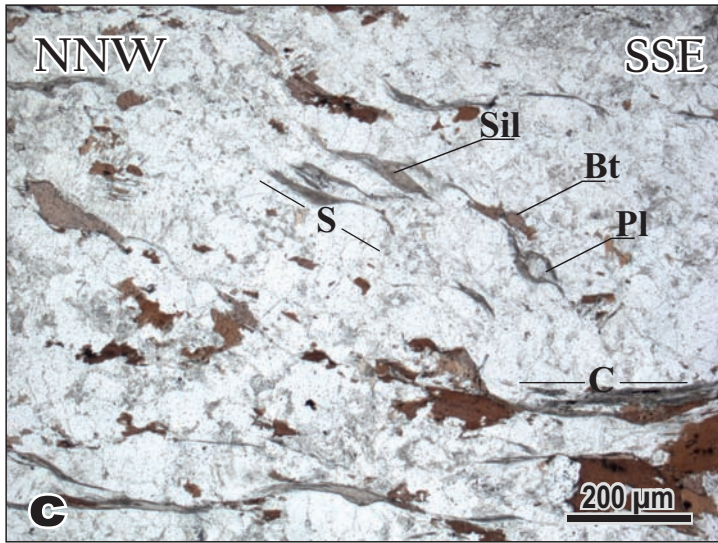
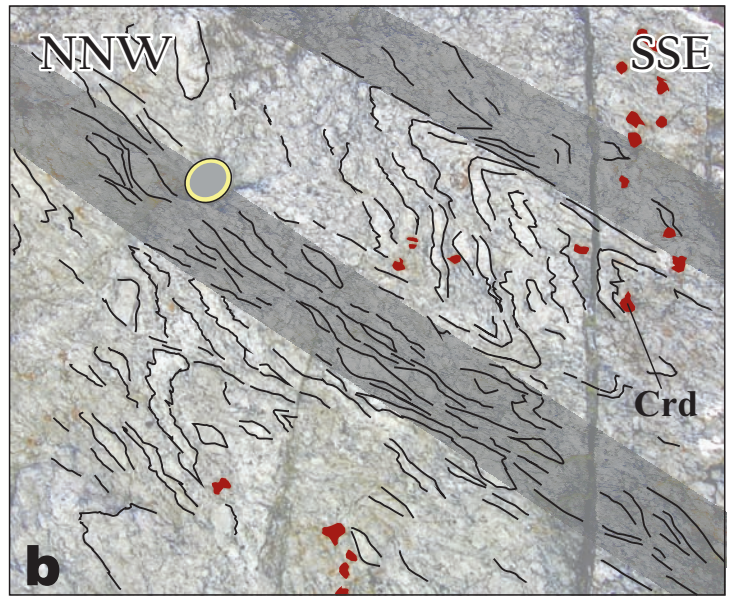
1197 **Figure. 12.** Age versus U concentration of all analyzed zircons as a function of sample.

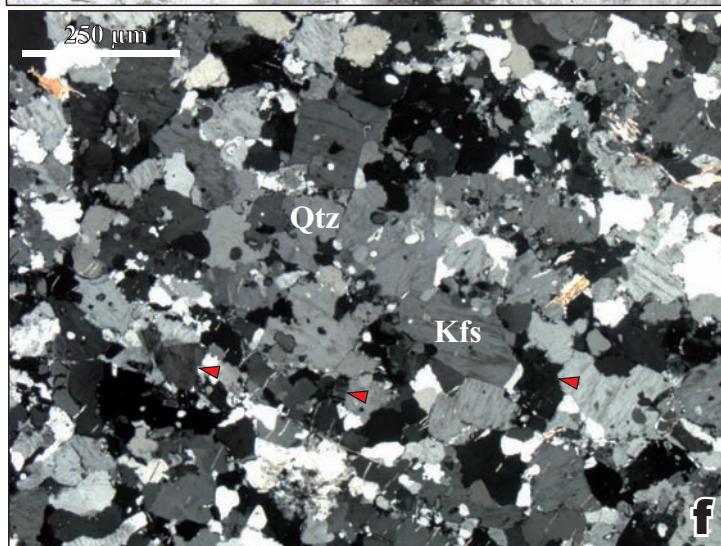
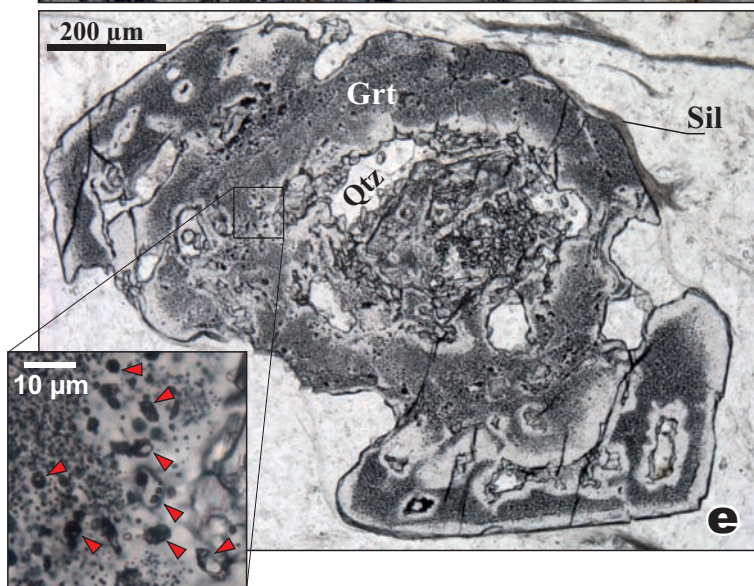
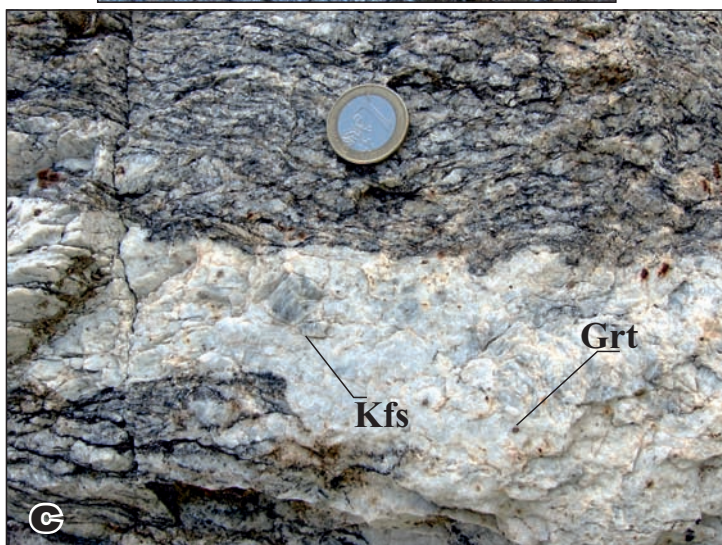
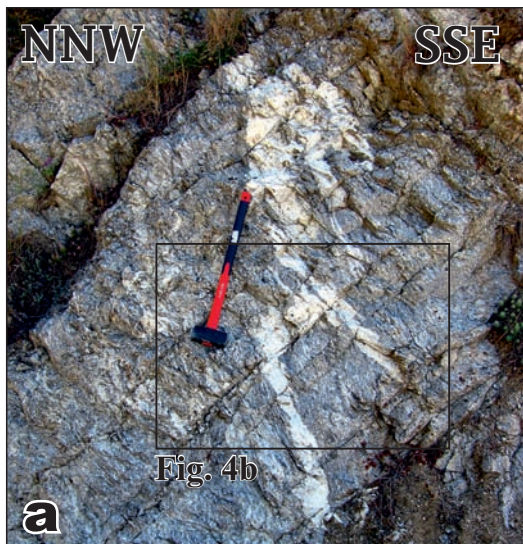


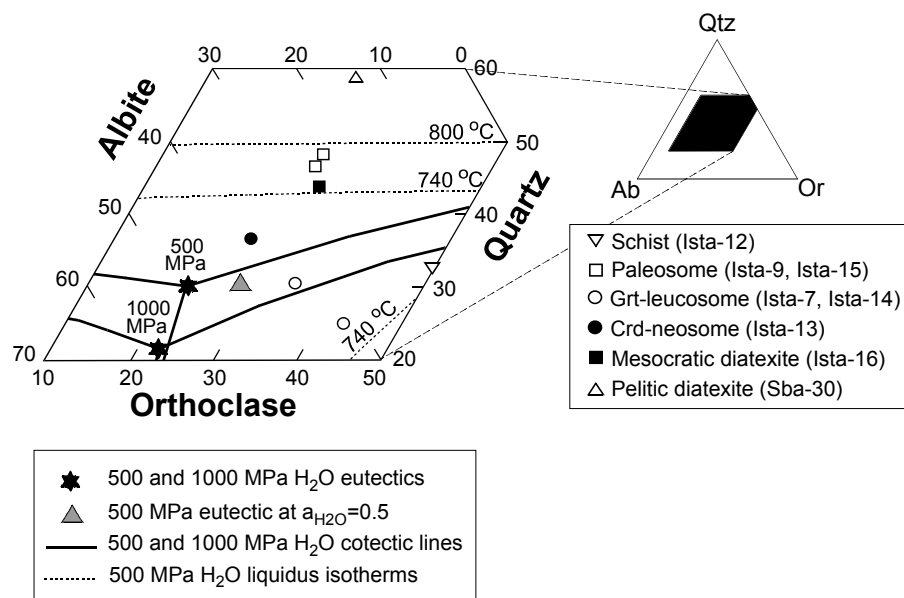
Acosta-Vigil et al. Fig. 1



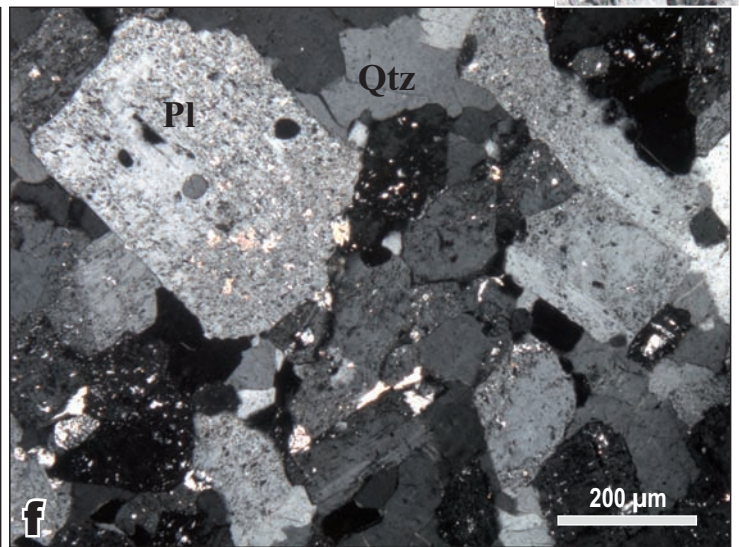
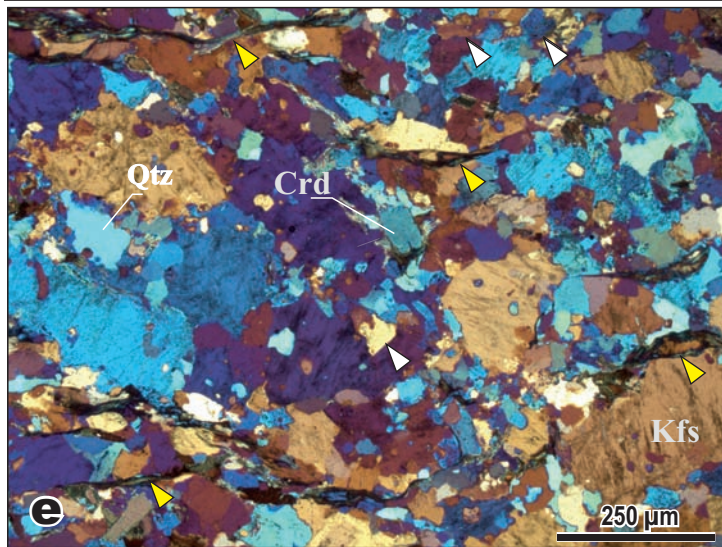
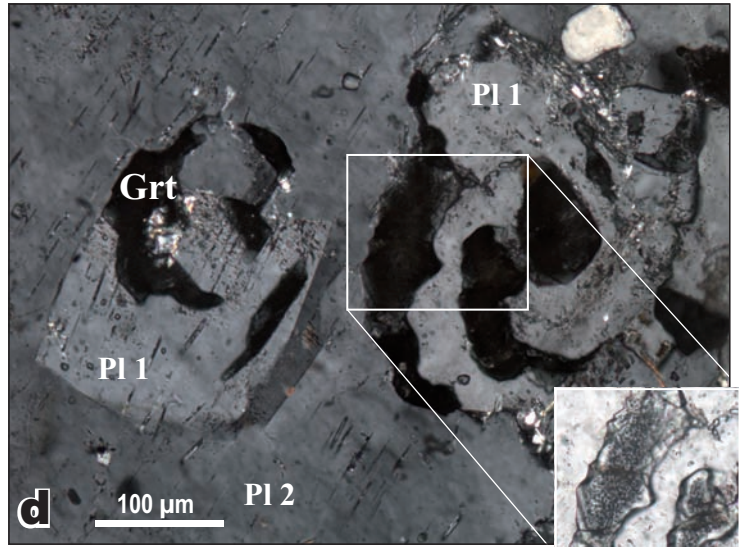
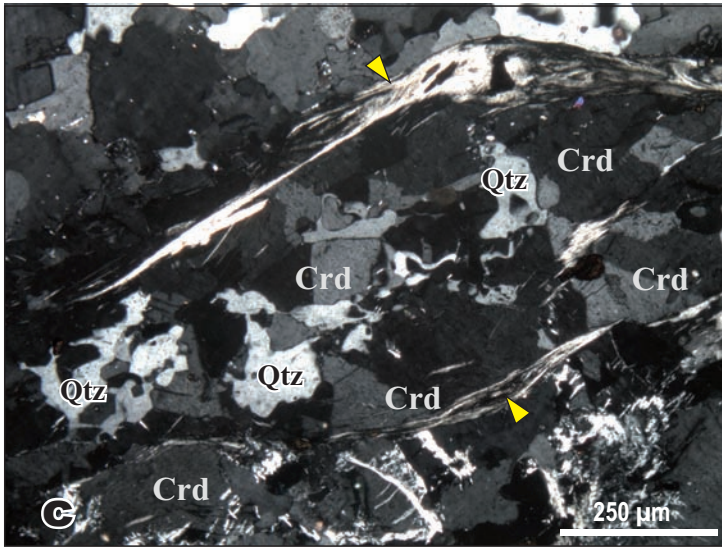
Acosta-Vigil et al. Fig. 2

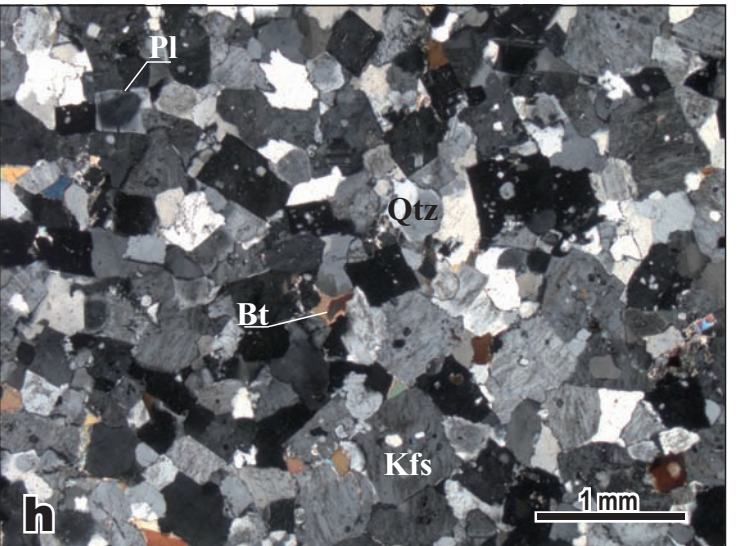
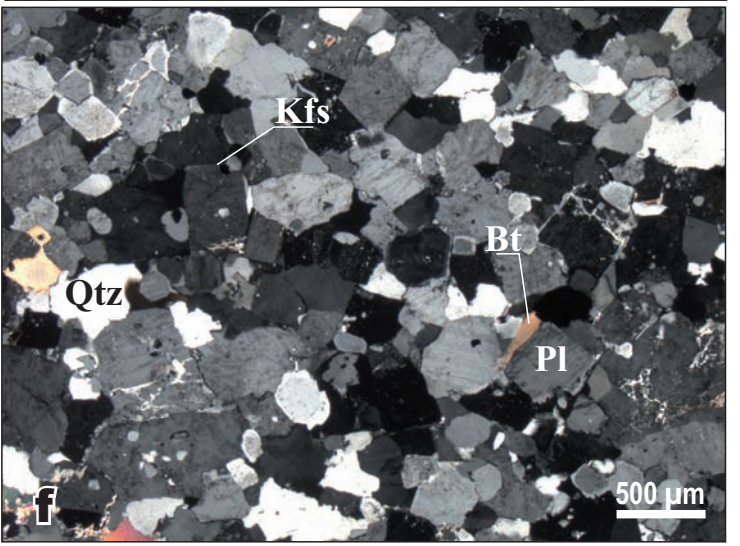






Acosta-Vigil et al. Fig. 5





Increasing time, temperature and proximity to the peridotites



• Grt ◊ Kfs ◊ Crd

▨ Paleosome (Orthogneiss)

◊ Grt-leucosomes

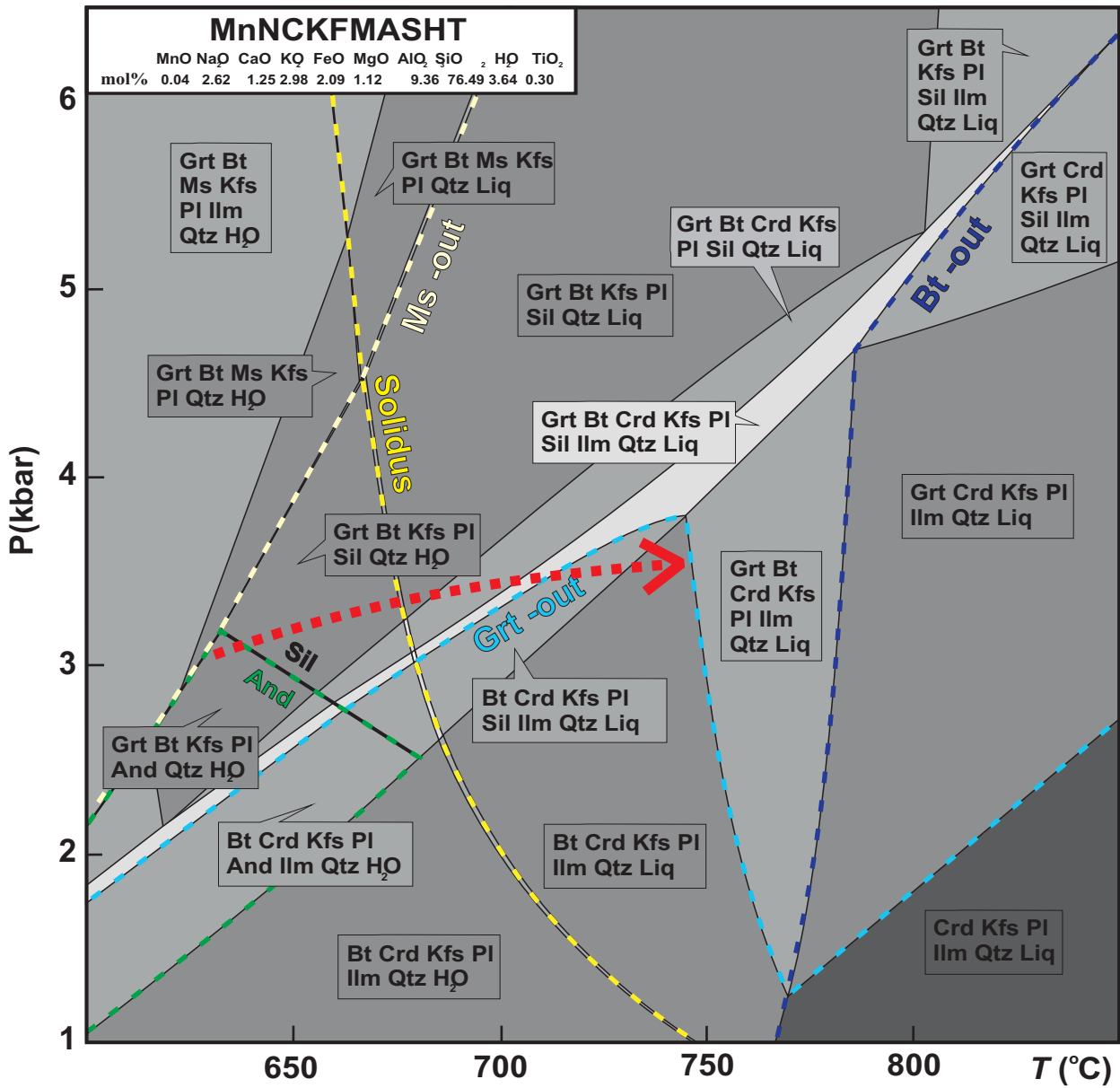
◊ Crd-neosomes

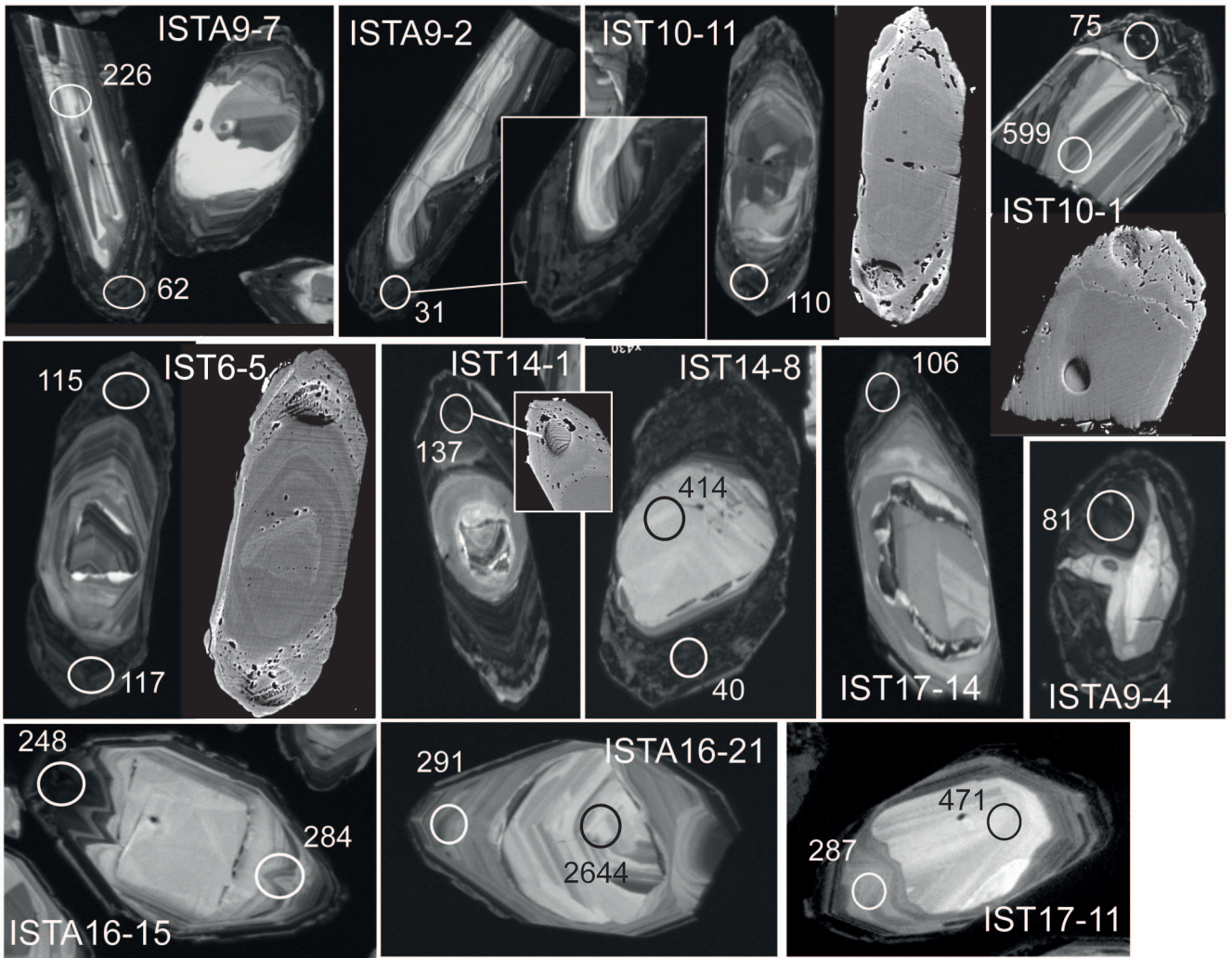
l. m. Diatexite

l. Leucocratic
m. Mesocratic

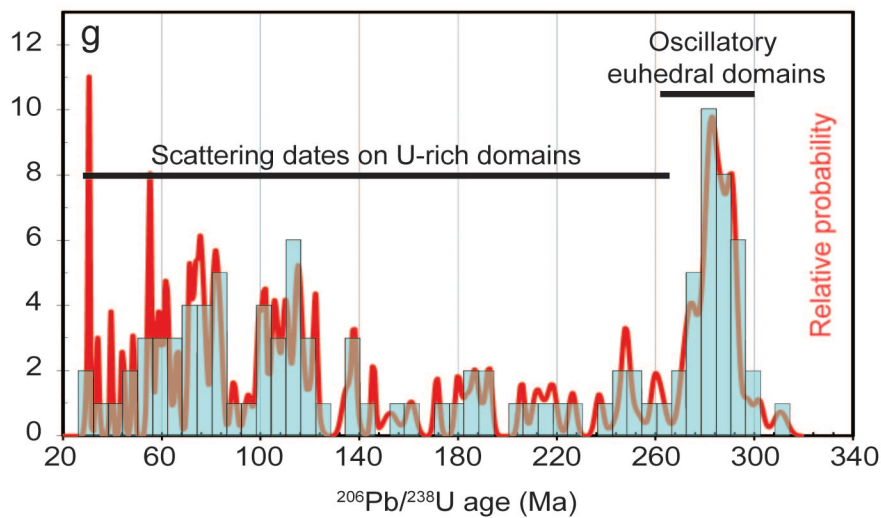
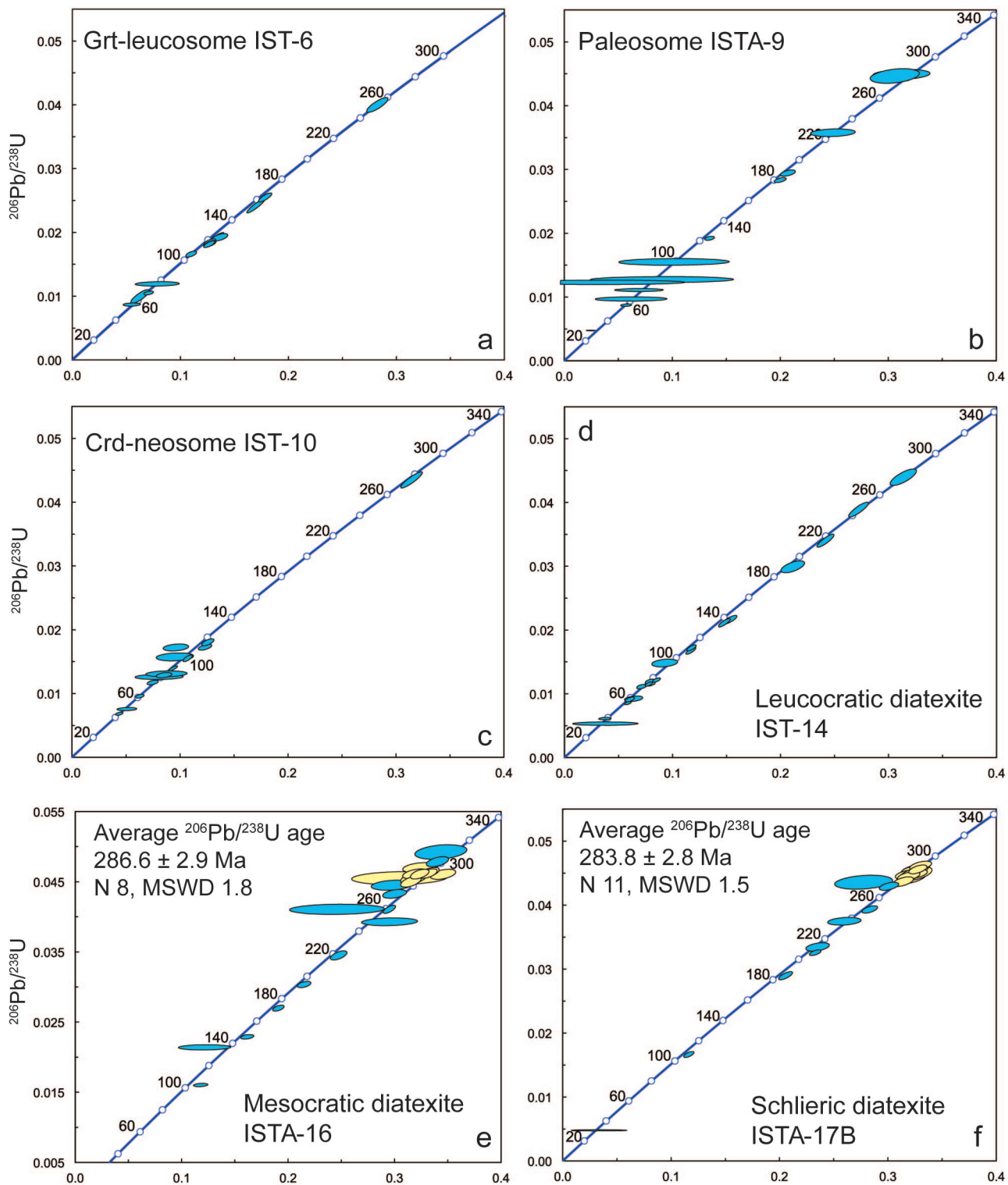
MnNCKFMASHT

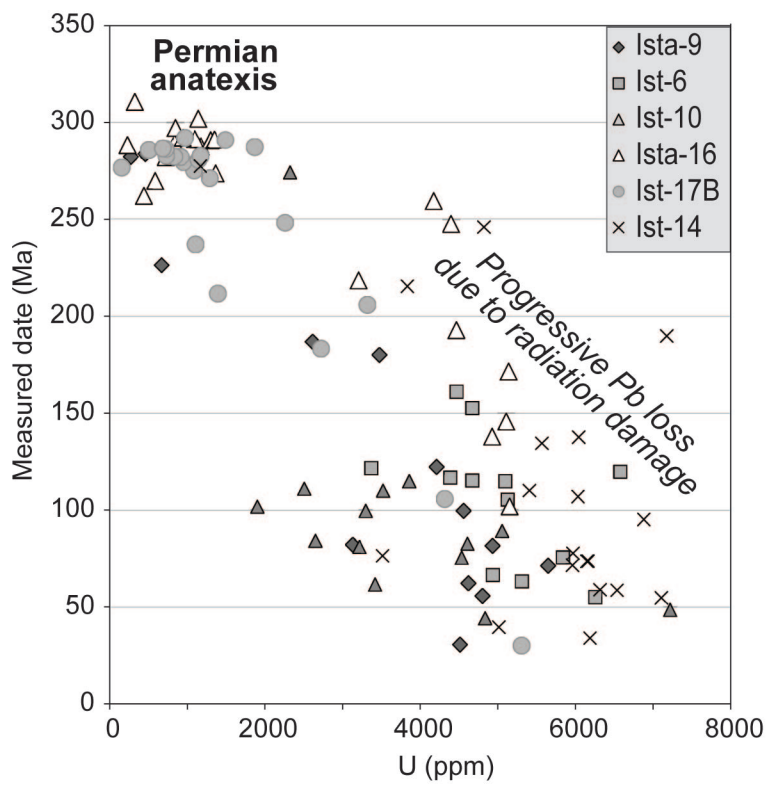
	MnO	Na ₂ O	CaO	K ₂ O	FeO	MgO	Al ₂ O ₃	SiO ₂	H ₂ O	TiO ₂
mol%	0.04	2.62	1.25	2.98	2.09	1.12	9.36	76.49	3.64	0.30





Acosta-Vigil et al. Fig. 10





Acosta-Vigil et al. Fig. 12

Table 1

Previous geochronological data of the Betic-Rif orogen

Authors	Rock type	Unit	Outcrop	Method	Age ^a (Ma)
Loomis (1975)	Diatexite	Guadaiza	Estepona/Guadaiza	K-Ar on whole rock and Bt	30-81
Priem et al. (1979)	Leucogranite	Intrusive within SB ^b peridotites	Estepona	Rb-Sr on whole rock	22-23
	Mylonite	Ojén	Albornoque	Rb-Sr on whole rock-Bt pairs	16-19
	Mylonite	Ojén	Albornoque	K-Ar on Bt	19-20
Zeck et al. (1989a)	Schist/Gneiss	Sierra Tejada/Torrox	Cómpeta/Torrox	Rb-Sr on whole rock-Ms pairs	19-23
Zeck et al. (1989b)	Leucogranite	Intrusive in schist of eastern Alpujárrides	Sierra Cabrera	Rb-Sr on whole rock-Ms pairs	19-20
Monié et al. (1991)	Gneiss	Almuñécar, central Alpujárrides	Punta de la Mona	⁴⁰ Ar- ³⁹ Ar on Bt and Ms	19
	Carpholite-Qtz lens	Trevenque, central Alpujárrides	?	⁴⁰ Ar- ³⁹ Ar on Ms	25
Zeck et al. (1992)	Schist/Gneiss	Sierra Tejada	Torrox	Rb-Sr on whole rock-Ms pairs	19-23
	Schist/Gneiss	Sierra Tejada	Torrox	⁴⁰ Ar- ³⁹ Ar on Bt	19-20
	Schist/Gneiss	Sierra Tejada	Torrox	⁴⁰ Ar- ³⁹ Ar on Ms	19
	Leucogranite	Intrusive in schist of eastern Alpujárrides	Sierra Cabrera	⁴⁰ Ar- ³⁹ Ar on Ms	18
Monié et al. (1994)	Amphibolite/Marble	Sierra Tejada/Ojén	Cómpeta/Albornoque	⁴⁰ Ar- ³⁹ Ar on amphibole	19
	Gneiss/Marble/Granulite/Granite	Torrox/Guadaiza/Los Reales/Intrusive in SA ^c peridotites	Torrox/Estepona/Albornoque/Jubrique	⁴⁰ Ar- ³⁹ Ar on Bt	19-22
	Schist/Gneiss	Sierra Tejada/Torrox/Los Reales	Cómpeta/Torrox/Yunquera	⁴⁰ Ar- ³⁹ Ar on Ms	19-20
Andriessen & Zeck (1996)	Gneiss	Torrox	Torrox	⁴⁰ Ar- ³⁹ Ar on Kfs	19-20
	Schist	Torrox	Torrox	Fission-track on Zrn and Ap	16-17
Acosta (1998)	Diatexite	Guadaiza	Estepona	Pb on Zrn, Kober method	315-335
Sánchez-Rodríguez (1998)	Diatexite	Guadaiza	Guadaiza	U-Pb on Zrn, SHRIMP	20, 304
	Leucogranite	Ojén	Undeformed cross-cutting vein in mylonites	U-Pb on Zrn, SHRIMP	20, 306
	Metatexite	Ojén	Albornoque	U-Pb on Zrn, SHRIMP	20, 291
	Granulite (leucosome)	Los Reales	Albornoque	U-Pb on Zrn, SHRIMP	21, 313
	Granulite (melanosome)	Los Reales	Beni Bousera	U-Pb on Zrn, SHRIMP	22, 296
	Leucogranite	Intrusive within SB ^b peridotites	Jubrique	U-Pb on Zrn, SHRIMP	19
Platt et al. (1998)	Schist/Migmatite		Basement of central-western Alborán Sea	⁴⁰ Ar- ³⁹ Ar on Bt and Ms	19-20
	Schist/Migmatite/Granite		Basement of central-western Alborán Sea	Fission-track on Ap	15-21
Sosson et al. (1998)	Migmatite/Granite	Ojén/Intrusive within SA ^c peridotites	Albornoque	⁴⁰ Ar- ³⁹ Ar on Bt and Ms	19
	Migmatite/Granite	Ojén/Intrusive within SA ^c peridotites	Albornoque	Fission-track on Ap	16-18
Platt & Whitehouse (1999)	Granulite	Los Reales	Carratraca	U-Pb on Zrn, Ion Microprobe	20-259
	Migmatite (leucosome)	Los Reales	Carratraca	U-Pb on Zrn, Ion Microprobe	23-302
	Gneiss	Guadaiza	Carratraca	U-Pb on Zrn, Ion Microprobe	20-255
	Gneiss	Adra or Herradura? Central Alpujárrides	Punta de la Mona	U-Pb on Zrn, Ion Microprobe	19-20
	Gneiss/Leucogranite	Carboneras fault zone, eastern Alpujárrides	Sierra Cabrera	U-Pb on Zrn, Ion Microprobe	19-24
Zeck & Whitehouse (1999)	Gneiss	Torrox	Torrox	U-Pb on Zrn, Ion Microprobe	285
Montel et al. (2000)	Granulite, including leucosome	Los Reales	Beni Bousera	U-Pb-Th on Mnz, Electron Probe	≤30, 284
Sánchez-Rodríguez & Gebauer (2000)	Eclogite	Ojén	Albornoque	U-Pb on Zrn, SHRIMP	20, 183
	Pyroxenite	Intrusive within SB ^b peridotites	Jubrique	U-Pb on Zrn, SHRIMP	131, 143, 178
	Leucogranite	Intrusive within SB ^b peridotites	Jubrique	U-Pb on Zrn, SHRIMP	19
Zeck & Williams (2001)	Shist	Eastern Alpujárrides?	Sierra Alhamilla	U-Pb on Zrn, SHRIMP	20, 305
Zeck & Whitehouse (2002)	Schist	Torrox	Torrox	U-Pb on Zrn, Ion Microprobe	313

^a Only Variscan or younger ages are reported. ^b SB=Sierra Bermeja. ^c SA=Sierra Alpujata

Table 1 (continuation)

Previous geochronological data of the Betic-Rif orogen

Authors	Rock type	Unit	Outcrop	Method	Age ^a (Ma)
Platt et al. (2003a)	Mafic granulite	Los Reales	Carratraca	⁴⁰ Ar- ³⁹ Ar on Hbl	20
	Quartzite/Schist/Gneiss/Migmatite/Granulite	Los Reales	Carratraca	⁴⁰ Ar- ³⁹ Ar on Bt	20-21
	Qtz vein/Quartzite/Schist/Migmatite	Los Reales	Carratraca	⁴⁰ Ar- ³⁹ Ar on Ms	20-22
	Psammite/Quartzite/Schist/Gneiss/Granulite	Los Reales	Carratraca	Fission-track on Zrn	19-22
	Greywacke/Quartzite/Schist/Gneiss/Migmatite/Granulite	Los Reales	Carratraca	Fission-track on Ap	15-25
Platt et al. (2003b)	Granulite	Los Reales	Jubrique/Beni Bousera	U-Pb on Zrn, Ion Microprobe	22-23
Whitehouse & Platt (2003)	Granulite	Los Reales	Carratraca	U-Pb on Zrn, Ion Microprobe	20-63
Platt et al. (2005)	Qtz-Phyllite	Salobreña? Eastern Alpujarrides	Sierra Alhamilla	⁴⁰ Ar- ³⁹ Ar on white mica	48
	Qtz-Phyllite	Salobreña? Eastern Alpujarrides	Sierra Alhamilla	Fission-track on Zrn	19
	Qtz-Phyllite	Lújar-Gádor? Eastern Alpujarrides	Charches	⁴⁰ Ar- ³⁹ Ar on white mica	45-85
	Phyllite	Salobreña or Adra? Eastern Alpujarrides	Eastern Sierra de las Estancias	⁴⁰ Ar- ³⁹ Ar on white mica	30-33
	Phyllite	Salobreña or Adra? Eastern Alpujarrides	Eastern Sierra de las Estancias	Fission-track on Zrn and Ap	18
Janots et al. (2006)	Qtz-Ky veins in schist	Beni Mzala, Upper Sebtides, Rif, Morocco	Beni Mzala	U-Th-Pb on Zrn, Ion Microprobe	21
Michard et al. (2006)	Schist	Beni Mzala, Upper Sebtides, Rif, Morocco	Beni Mzala	K-Ar and ⁴⁰ Ar- ³⁹ Ar on white mica	21-29
	Schist	Filali, Lower Sebtides, Rif, Morocco	Beni Bousera	K-Ar on Bt	21
Rossetti et al. (2010)	Granulite (leucosome)	Beni Bousera, Lower Sebtides, Rif, Morocco	Oued 'Mter	U-Pb on Zrn, LA-ICP-MS	23, 305
	Slightly discordant granitic sheets in granulite & gneiss (leptinites)	Beni Bousera & Filali, Lower Sebtides, Rif, Morocco	Oued 'Mter	U-Pb on Zrn and Mnz, LA-ICP-MS	22, 301
	Slightly discordant granitic sheets in gneiss (leptinites)	Filali, Lower Sebtides, Rif, Morocco	Oued 'Mter	U-Pb on Mnz, LA-ICP-MS	21
	Leucogranite dikes in gneisses	Filali, Lower Sebtides, Rif, Morocco	Oued 'Mter	U-Pb on Zrn and Mnz, LA-ICP-MS	21-23
	Leucogranite dikes in granulite and gneiss	Beni Bousera & Filali, Lower Sebtides, Rif, Morocco	Oued 'Mter	⁴⁰ Ar- ³⁹ Ar on Bt and Ms	21-22
Esteban et al. (2011a)	Mylonite/Leucogranite/Granite	Guadaiza/Intrusive within SB ^b and SA ^c peridotites	Guadaiza/Peñas Blancas/Albornoque	U-Pb on Zrn, SHRIMP	19-43
Esteban et al. (2011b)	Mylonite/Metaquartzite	Guadaiza/Ojén	Yunqueira/Sierra de Mijas	U-Pb on Zrn, SHRIMP	20-22

^a Only Variscan or younger ages are reported. ^b SB=Sierra Bermeja. ^c SA=Sierra Alpujata

Table 2

Bulk rock major element (wt%) and trace element (ppm) concentrations of rocks from the Guadaiza Unit

Lable	ISTA-12	ISTA-9	ISTA-15	ISTA-7	ISTA-14	ISTA-13	ISTA-16	SBA-30
Lithology	Schist	Paleosome	Paleosome	Grt-Lcs	Grt-Lcs	Crd-Neos	Meso Diatexite	Pel Diatexite
SiO ₂	54.76	75.80	75.34	72.04	74.88	73.61	72.96	66.13
Al ₂ O ₃	23.10	13.90	13.22	16.15	14.53	16.20	15.16	17.82
TiO ₂	1.07	0.26	0.26	0.02	0.01	0.03	0.38	0.94
FeO*	7.44	1.58	1.79	0.21	0.25	0.30	2.38	6.31
MnO	0.17	0.04	0.04	0.11	0.07	0.01	0.04	0.10
MgO	2.08	0.37	0.39	0.08	0.11	0.26	0.72	2.09
CaO	1.59	0.91	0.80	0.82	0.81	1.48	1.11	1.17
Na ₂ O	1.14	2.60	2.40	3.59	3.95	3.95	2.58	1.06
K ₂ O	5.15	4.40	4.38	6.98	5.68	4.01	4.46	3.09
P ₂ O ₅	0.16	0.26	0.30	0.31	0.28	0.35	0.25	0.19
LOI	2.78	0.69	0.72	0.36	0.36	0.62	1.04	1.56
Total	99.45	100.81	99.65	100.67	100.93	100.82	101.07	100.48
ASI	2.23	1.30	1.30	1.08	1.03	1.20	1.37	2.47
Mg#	0.46	0.29	0.28	0.40	0.44	0.61	0.35	0.37
K#	0.75	0.53	0.55	0.56	0.49	0.40	0.53	0.66
Rb	183	282	341	416	325	197	299	136
Sr	140	54	66	67	88	71	103	114
Ba	476	126	136	145	139	75	244	462
Sc	22	4.0	4.2	0.90	0.80	1.0	6.4	17
V	197	17	17	3.0	3.0	3.9	33	146
Cr	117	0.00	0.20	0.30	0.40	0.60	7.7	89
Y	16	8.9	12	3.5	4.8	4.4	16	16
Nb	19	13	15	1.6	0.76	55	13	17
Zr	n.d.	n.d.	94	n.d.	27	28	123	245
U	2.0	2.6	6.6	0.70	3.4	7.0	4.7	2.0
Th	14	6.2	8.5	0.40	0.20	3.4	10	13
T Zrn					650	663	787	
Th/U	7.0	2.4	1.3	0.57	0.06	0.49	2.1	6.7
Eu/Eu*	0.70	0.36	0.29	1.56	1.86	0.62	0.45	0.59
Sum REE	184	77	113	14	10	21	124	193

* Total Fe as FeO; Grt Lcs=Garnet leucosome; Crd Neos=Cordierite neosome; Meso=Mesocratic; Pel=Pelitic; n.d. not determined.

ASI=moles (Al₂O₃/(CaO+Na₂O+K₂O)); Mg#=moles (MgO/(MgO+FeO*)); K#=moles (K₂O/(K₂O+Na₂O))

T Zrn=Saturation zircon temperature (Watson and Harrison, 1983)

Supplementary Table 1

SHRIMP U-Pb analyses of zircon

Spot Name	% initial ²⁰⁶ Pb	U (ppm)	Th (ppm)	204Pb- corrected Concordia ratios					207Pb-corrected ratio and age					
				²³² Th/ ²³⁶ U	²⁰⁷ Pb/ ²³⁵ U	% error	% ²⁰⁶ Pb/ ²³⁸ U	% error	Error correlation	²⁰⁶ Pb/ ²³⁸ U	% error	²⁰⁶ Pb/ ²³⁸ U Age (Ma)	±1 σ	CL zone
ISTA9-3	0,89	4513	23	0,005	0,02819	6,38	0,00472	0,69	0,108	0,004789	0,63	30,5	0,2	dark rim
ISTA9-14	0,90	4803	53	0,011	0,06049	3,21	0,00870	0,77	0,240	0,008774	0,75	55,6	0,4	dark rim
ISTA9-7	3,92	4623	75	0,017	0,06489	20,59	0,00972	1,36	0,066	0,01014	1,04	62,3	0,9	dark mosaic rim
ISTA9-5	3,32	5647	43	0,008	0,07229	12,64	0,01111	0,82	0,065	0,01154	0,65	71,3	0,6	dark mosaic rim
ISTA9-4	4,70	4931	26	0,005	0,09285	28,92	0,01280	1,55	0,054	0,01336	0,87	81,5	1,4	dark rim
ISTA9-1	9,65	3134	27	0,009	0,03710	84,71	0,01239	1,30	0,015	0,01423	0,66	81,9	1,4	dark composite rim
ISTA9-12	2,23	4557	51	0,012	0,10183	20,24	0,01556	1,23	0,061	0,01597	0,80	99,6	1,1	dark rim
ISTA9-16	0,20	4213	61	0,015	0,13460	1,40	0,01921	0,59	0,421	0,01926	0,59	122,3	0,7	dark composite rim
ISTA9-8	0,11	3475	64	0,019	0,19921	1,11	0,02835	0,63	0,564	0,02839	0,62	179,9	1,1	dark rim
ISTA9-11	0,21	2614	53	0,021	0,20647	1,35	0,02943	0,69	0,515	0,02948	0,69	186,8	1,3	dark composite rim
ISTA9-7C	0,96	668	167	0,258	0,24749	3,40	0,03572	0,68	0,201	0,03586	0,66	226,4	1,5	oscillatory euhedral
ISTA9-15	0,20	271	86	0,330	0,30501	3,02	0,04463	1,08	0,355	0,04483	1,07	282,3	3,0	oscillatory euhedral
ISTA9-13	0,15	459	34	0,076	0,31123	3,48	0,04490	0,71	0,203	0,04505	0,68	283,7	1,9	oscillatory euhedral
ISTA9-6	0,93	409	106	0,269	0,48444	1,68	0,06403	0,92	0,544	0,06413	0,92	400,0	3,6	detrital core
ISTA9-10	0,10	523	207	0,408	0,68732	1,31	0,08548	0,84	0,640	0,08552	0,84	528,5	4,3	detrital core
ISTA9-2	0,30	263	58	0,228	0,70997	2,74	0,09299	0,72	0,263	0,09348	0,70	575,8	4,0	detrital core
IST6-2	1,29	6256	78	0,013	0,05537	5,89	0,00858	1,30	0,220	0,008687	1,26	55,0	0,7	dark rim
IST6-6	0,92	5310	312	0,061	0,06296	5,41	0,00984	4,45	0,823	0,009935	4,45	63,1	2,8	dark rim
IST6-2.1	1,09	4935	111	0,023	0,07086	2,52	0,01039	1,19	0,473	0,01047	1,18	66,4	0,8	dark rim
IST6-11	2,11	5841	86	0,015	0,07876	10,59	0,01181	1,30	0,122	0,01204	1,19	75,5	0,9	dark composite rim
IST6-10	0,58	5129	58	0,012	0,11035	1,94	0,01648	1,19	0,611	0,01657	1,18	105,3	1,2	dark oscillatory rim
IST6-1	0,73	5097	46	0,009	0,12695	1,68	0,01803	1,20	0,717	0,01810	1,20	114,8	1,4	dark mosaic rim
IST6-5	0,71	4671	57	0,013	0,12779	1,78	0,01811	1,18	0,664	0,01817	1,18	115,3	1,3	dark rim
IST6-5.1	0,67	4388	61	0,014	0,12740	1,77	0,01832	1,22	0,690	0,01839	1,22	116,7	1,4	dark oscillatory rim
IST6-3	0,49	6576	73	0,011	0,13200	2,57	0,01880	2,36	0,919	0,01883	2,36	119,7	2,8	dark oscillatory rim
IST6-6.1	0,77	3369	74	0,023	0,13706	2,13	0,01913	1,23	0,577	0,01920	1,23	121,6	1,5	dark composite rim
IST6-4	0,41	4670	67	0,015	0,17017	2,00	0,02402	1,84	0,918	0,02405	1,84	152,6	2,8	oscillatory rim
IST6-9	0,38	4469	30	0,007	0,17863	1,44	0,02535	1,18	0,818	0,02539	1,18	161,0	1,9	dark embajment
IST6-12	0,08	2652	183	0,071	0,28282	1,43	0,03986	1,18	0,823	0,03988	1,18	251,9	2,9	oscillatory
IST6-9C	0,18	199	33	0,173	0,61240	3,11	0,07917	1,31	0,420	0,07940	1,30	491,7	6,3	detrital core
IST6-7	0,00	668	39	0,060	0,82130	1,59	0,10152	1,20	0,756	0,10162	1,20	624,7	7,3	detrital core
IST6-8	0,00	1188	43	0,037	0,86857	1,41	0,10531	1,19	0,842	0,10539	1,19	646,5	7,5	detrital core
IST10-9	0,57	4835	50	0,011	0,04593	3,08	0,00689	1,57	0,508	0,006913	1,56	44,2	0,7	dark mosaic rim
IST10-13	9,20	7221	69	0,010	0,05325	7,21	0,00761	1,25	0,173	0,008316	1,18	48,5	0,6	dark composite rim
IST10-5	0,63	3418	14	0,004	0,06486	2,55	0,00961	1,26	0,494	0,009648	1,25	61,5	0,8	dark mosaic rim
IST10-1	0,72	4533	21	0,005	0,07711	2,51	0,01177	1,19	0,474	0,01185	1,18	75,4	0,9	dark mosaic rim
IST10-2	3,95	3218	29	0,009	0,08260	10,96	0,01264	1,31	0,120	0,01315	1,19	80,9	1,0	dark mosaic rim

corrected ²⁰⁷Pb/²⁰⁶Pb ratio and age given

Supplementary Table 1 (continuation 1)

SHRIMP U-Pb analyses of zircon

Spot Name	% initial ²⁰⁶ Pb	U (ppm)	Th (ppm)	204Pb- corrected Concordia ratios					207Pb-corrected ratio and age					
				²³² Th/ ²³⁶ U	²⁰⁷ Pb/ ²³⁵ U	% error	% ²⁰⁶ Pb/ ²³⁸ U	% error	Error correlation	²⁰⁶ Pb/ ²³⁸ U	% error	²⁰⁶ Pb/ ²³⁸ U Age (Ma)	±1 σ	CL zone
IST10-10	0,53	4609	17	0,004	0,08742	3,40	0,01291	1,28	0,376	0,01296	1,27	82,6	1,1	dark rim
IST10-7	1,03	2649	28	0,011	0,08912	8,65	0,01316	1,28	0,148	0,01327	1,20	84,1	1,0	dark mosaic rim
IST10-6	0,42	5055	44	0,009	0,09577	1,62	0,01396	1,31	0,813	0,01398	1,31	89,1	1,2	dark mosaic rim
IST10-3	0,43	3298	39	0,012	0,10893	1,61	0,01561	1,18	0,734	0,01563	1,18	99,5	1,2	dark composite rim
IST10-4	0,20	1903	13	0,007	0,09737	6,96	0,01583	1,54	0,221	0,01593	1,49	101,6	1,5	dark mosaic rim
IST10-11	0,51	3523	25	0,007	0,12292	2,01	0,01729	1,21	0,602	0,01730	1,21	110,0	1,3	dark composite rim
IST10-14	0,44	2506	27	0,011	0,09743	4,94	0,01722	1,34	0,272	0,01744	1,32	111,0	1,5	mosaic dark rim
IST10-4.1	0,55	3858	38	0,010	0,12617	1,78	0,01803	1,19	0,667	0,01807	1,19	114,8	1,4	mosaic rim
IST10-12	0,05	2323	437	0,195	0,31349	1,31	0,04348	1,18	0,902	0,04347	1,18	274,2	3,2	oscillatory
IST10-1C	0,00	270	131	0,501	0,80255	1,56	0,09741	1,23	0,790	0,09740	1,23	599,3	7,2	detrital core
IST10-8 #	3,38	3815	361	0,098	4,11736	1,28	0,25387	1,22	0,953	0,1176	0,39	1920	7	detrital core/dimain
ISTA16-10	0,65	5153	43	0,009	0,11741	2,38	0,016019	0,59	0,249	0,01613	0,58	101,8	0,6	dark rim
ISTA16-9	0,91	4927	38	0,008	0,12120	8,26	0,021413	0,67	0,081	0,02188	0,59	137,9	0,8	dark rim
ISTA16-16	0,22	5110	53	0,011	0,16103	1,57	0,022913	0,59	0,373	0,02299	0,58	145,7	0,8	dark oscillatory rim
ISTA16-18	9,25	5137	783	0,157	0,19033	1,14	0,027008	0,63	0,558	0,02706	0,63	171,5	1,1	dark rim
ISTA16-11	0,09	4464	24	0,006	0,21430	1,23	0,030391	0,60	0,485	0,03046	0,59	192,7	1,1	dark oscillatory rim
ISTA16-2	0,14	3205	60	0,019	0,24690	1,27	0,034533	0,76	0,601	0,03459	0,76	218,5	1,7	oscillatory rim
ISTA16-15	1,70	4400	33	0,008	0,29484	3,65	0,039323	0,59	0,161	0,03990	0,58	247,7	1,5	dark oscillatory rim
ISTA16-8	0,05	4174	19	0,005	0,29440	0,82	0,041098	0,58	0,706	0,04112	0,58	259,5	1,5	dark embajment
ISTA16-17	0,55	438	20	0,047	0,24538	7,41	0,041075	0,76	0,103	0,04166	0,68	262,1	1,8	dark embajment
ISTA16-13	0,11	1365	35	0,027	0,29944	1,55	0,043293	0,61	0,394	0,04341	0,61	273,7	1,6	unzoned rim
ISTA16-6	0,02	722	18	0,026	0,29682	2,66	0,044525	0,65	0,246	0,04467	0,64	282,0	1,8	oscillatory rim
ISTA16-15A	0,03	845	30	0,036	0,31486	1,26	0,045047	0,70	0,559	0,04511	0,70	284,5	2,0	oscillatory rim
ISTA16-22	0,59	229	75	0,341	0,30379	6,01	0,045516	0,85	0,141	0,04579	0,78	288,2	2,3	oscillatory core
ISTA16-5	0,00	1175	44	0,039	0,31749	1,57	0,045537	0,76	0,484	0,04564	0,76	287,6	2,2	oscillatory rim
ISTA16-19	0,09	835	27	0,033	0,34503	1,42	0,046048	0,63	0,445	0,04607	0,63	289,4	1,8	oscillatory rim
ISTA16-3	0,01	1299	29	0,023	0,32290	1,12	0,046070	0,61	0,539	0,04612	0,60	290,8	1,7	oscillatory core
ISTA16-21	0,02	1099	29	0,027	0,31933	1,58	0,046109	0,62	0,394	0,04619	0,62	291,3	1,8	oscillatory core
ISTA16-23	0,08	1347	96	0,073	0,33067	1,10	0,046189	0,61	0,556	0,04623	0,61	291,2	1,8	oscill/unzoned rim
ISTA16-14	0,00	940	39	0,042	0,33202	1,16	0,046338	0,62	0,538	0,04634	0,62	292,1	1,8	oscillatory rim
ISTA16-7	0,02	845	29	0,035	0,32289	2,00	0,047034	0,63	0,317	0,04719	0,63	297,2	1,8	oscillatory rim
ISTA16-4	0,04	1141	38	0,035	0,33980	1,24	0,047894	0,61	0,495	0,04794	0,61	301,9	1,8	oscillatory rim
ISTA16-7C	0,27	323	52	0,167	0,34282	2,90	0,049232	0,87	0,301	0,04945	0,86	310,6	2,7	detrital core
ISTA16-20	1,42	528	29	0,056	0,50722	1,96	0,055361	0,67	0,342	0,05550	0,66	341,8	2,4	detrital unzoned
ISTA16-2C #	0,06	1225	64	0,054	8,50672	0,65	0,394711	0,59	0,909	0,1563	0,27	2416	5	detrital core
ISTA16-21C #	0,00	414	157	0,391	12,24110	1,15	0,495910	0,79	0,690	0,1790	0,83	2644	14	detrital core
IST17-15.1	8,10	5306	24	0,005	0,03272	32,08	0,00471	0,80	0,025	0,005124	0,80	30,1	0,7	dark rim
IST17-14.1	0,24	4319	43	0,010	0,11555	1,66	0,01657	1,15	0,692	0,01661	1,15	105,6	1,2	dark composite rim
IST17-2.2	0,12	2723	32	0,012	0,20479	1,25	0,02892	0,91	0,726	0,02895	0,91	183,4	1,6	dark oscillatory rim
IST17-10.1	0,12	3317	37	0,012	0,23232	0,96	0,03250	0,58	0,605	0,03254	0,58	205,8	1,2	dark oscillatory rim
IST17-19.1	0,36	1393	39	0,029	0,23434	1,90	0,03341	0,82	0,432	0,03353	0,82	211,7	1,7	oscillatory
IST17-4.1	0,98	1106	24	0,023	0,25900	2,44	0,03745	0,64	0,264	0,03782	0,64	237,2	1,5	dark composite rim
IST17-21.1	0,05	2260	31	0,014	0,28235	1,05	0,03930	0,61	0,582	0,03932	0,61	248,2	1,5	oscillatory rim
IST17-12.1	0,10	1289	49	0,039	0,30037	1,23	0,04292	0,63	0,512	0,04296	0,63	271,2	1,7	oscillatory rim

corrected ²⁰⁷Pb/²⁰⁶Pb ratio and age given

Supplementary Table 1 (continuation 2)

SHRIMP U-Pb analyses of zircon

Spot Name	204Pb- corrected Concordia ratios									207Pb-corrected ratio and age				
	% initial ²⁰⁶ Pb	U (ppm)	Th (ppm)	²³² Th/ ²³⁶ U	²⁰⁷ Pb/ ²³⁵ U	% error	% ²⁰⁶ Pb/ ²³⁸ U	% error	Error correlation	²⁰⁶ Pb/ ²³⁸ U	% error	²⁰⁶ Pb/ ²³⁸ U Age (Ma)	±1 σ	CL zone
IST17-15.2	0,85	158	141	0,924	0,27684	3,94	0,04355	1,04	0,263	0,04392	1,04	276,7	2,9	oscillatory core
IST17-6.1	0,06	1088	36	0,034	0,31290	1,28	0,04363	0,70	0,545	0,04366	0,70	275,2	1,9	oscillatory rim
IST17-17.1	0,11	954	28	0,030	0,32112	1,76	0,04435	0,93	0,532	0,04440	0,93	279,5	2,6	oscillatory rim
IST17-20.1	0,07	1141	29	0,026	0,31848	1,33	0,04451	0,68	0,512	0,04454	0,68	280,7	1,9	oscillatory rim
IST17-16.1	0,26	896	26	0,030	0,31810	1,53	0,04474	0,67	0,442	0,04486	0,67	282,3	1,9	oscillatory rim
IST17-8.1	0,04	914	28	0,031	0,32101	1,45	0,04476	0,88	0,608	0,04478	0,88	282,3	2,5	oscillatory rim
IST17-5.1	0,03	832	24	0,029	0,32489	1,36	0,04481	0,65	0,478	0,04482	0,65	282,4	1,8	oscillatory rim
IST17-7.1	0,03	1168	32	0,029	0,31997	1,34	0,04483	0,85	0,632	0,04485	0,85	282,8	2,4	oscillatory rim
IST17-18.1	0,03	729	20	0,029	0,32699	1,64	0,04489	0,92	0,560	0,04491	0,92	282,8	2,6	oscillatory rim
IST17-6.2	0,05	505	11	0,022	0,32497	1,71	0,04533	0,72	0,420	0,04535	0,72	285,8	2,0	oscillatory rim
IST17-9.1	0,10	725	29	0,041	0,32367	1,55	0,04541	0,70	0,454	0,04545	0,70	286,4	2,0	oscillatory rim
IST17-11.2	0,09	683	17	0,026	0,32403	1,59	0,04545	0,81	0,509	0,04549	0,81	286,6	2,3	oscillatory rim
IST17-22.1	0,03	1870	90	0,050	0,32667	1,05	0,04556	0,61	0,583	0,04557	0,61	287,2	1,7	oscillatory rim
IST17-3.1	0,25	1490	38	0,026	0,32935	1,26	0,04615	0,64	0,505	0,04627	0,64	291,0	1,8	oscillatory rim
IST17-11.1	0,72	138	61	0,458	0,53779	3,01	0,07528	1,08	0,359	0,07582	1,08	470,5	5,0	detrital core
IST17-16.2	0,64	95	51	0,555	0,65387	3,19	0,08549	1,15	0,360	0,08604	1,15	530,4	6,0	detrital core
IST17-2.1	0,14	328	173	0,545	0,78192	1,45	0,09691	0,74	0,511	0,09705	0,74	597,2	4,3	detrital core
IST17-4.2	0,79	23	27	1,241	0,80962	5,43	0,10105	2,02	0,371	0,10186	2,02	622,4	12,4	detrital core
IST17-19.2	0,74	147	33	0,228	1,01128	3,04	0,12087	0,99	0,326	0,12178	0,99	738,4	7,2	detrital core
IST17-17.2#	0,22	190	97	0,531	1,90965	1,43	0,18121	0,85	0,594	0,07555	1,65	1072	9	detrital core
IST17-13.1#	0,67	223	291	1,348	5,51320	1,44	0,34698	1,16	0,807	0,11994	0,61	1927	22	detrital core
IST14-8.2	3,69	6191	29	0,005	0,037507	32,82	0,005316	2,27	0,069	0,005483	1,47	34,0	0,6	dark mosaic rim
IST14-8	1,15	5015	22	0,004	0,037118	6,37	0,006135	1,26	0,198	0,006227	1,23	39,6	0,5	dark mosaic rim
IST14-16	0,58	7109	21	0,003	0,058313	2,15	0,008543	1,19	0,552	0,008566	1,19	54,7	0,6	dark mosaic rim
IST14-2	0,69	6538	66	0,010	0,060246	2,94	0,009128	1,72	0,585	0,009182	1,72	58,5	1,0	dark mosaic rim
IST14-6	4,26	6317	49	0,008	0,063732	5,31	0,009214	1,96	0,370	0,009576	1,94	58,8	1,1	dark mosaic/oscill rim
IST14-7	0,57	5963	39	0,007	0,071298	2,66	0,011142	1,33	0,499	0,01122	1,32	71,5	0,9	dark mosaic rim
IST14-16.2	0,53	6149	16	0,003	0,078187	1,77	0,011501	1,18	0,668	0,01153	1,18	73,5	0,9	dark mosaic/oscill rim
IST14-3	0,57	6162	45	0,008	0,079038	2,52	0,011516	1,19	0,474	0,01155	1,19	73,6	0,9	dark mosaic rim
IST14-4	0,28	3514	36	0,011	0,079099	2,25	0,011932	1,29	0,573	0,01196	1,28	76,4	1,0	dark mosaic rim
IST14-14	0,70	5968	63	0,011	0,085077	1,76	0,012168	1,19	0,676	0,01220	1,19	77,7	0,9	dark mosaic rim
IST14-13	0,87	6881	88	0,013	0,092687	5,38	0,014816	1,66	0,309	0,01499	1,64	95,1	1,6	dark oscillatory rim
IST14-5	0,44	6031	29	0,005	0,116812	1,60	0,016767	1,27	0,792	0,01679	1,27	106,9	1,4	dark rim
IST14-12	0,35	5407	57	0,011	0,117144	1,61	0,017239	1,18	0,732	0,01728	1,18	110,0	1,3	dark mosaic rim
IST14-11	0,39	5569	84	0,016	0,147709	1,51	0,021133	1,27	0,844	0,02116	1,27	134,5	1,7	dark mosaic/oscill rim
IST14-1	0,38	6041	80	0,014	0,152871	1,68	0,021637	1,34	0,798	0,02165	1,34	137,6	1,8	dark mosaic rim
IST14-18	0,82	7176	114	0,016	0,210823	2,10	0,029941	1,29	0,617	0,03014	1,29	189,9	2,4	dark mosaic rim
IST14-9	0,19	3834	15	0,004	0,241578	1,35	0,034030	1,18	0,871	0,03405	1,18	215,4	2,5	dark rim
IST14-15	0,07	4820	315	0,068	0,271853	1,36	0,038878	1,18	0,869	0,03892	1,18	246,0	2,9	dark oscillatory rim
IST14-10	0,06	1166	49	0,043	0,313409	1,60	0,043975	1,21	0,757	0,04401	1,21	277,5	3,3	unzoned rim
IST14-8C	0,95	247	41	0,173	0,511197	4,22	0,066241	1,32	0,312	0,06680	1,29	413,0	5,3	detrital core

corrected ²⁰⁷Pb/²⁰⁶Pb ratio and age given